Syntaxin11 Deficiency Inhibits CRAC Channel Priming to Suppress Cytotoxicity and Gene Expression in FHLH4 Patient T Lymphocytes.

Sritama Datta[1#], Abhikarsh Gupta[1#], Kunal Mukesh Jagetiya[1], Atharva Rahul Yande[1], Vikas Tiwari[2⊥], Megumi Yamashita[3⊥], Resmi Bera[1], Sandra Ammann[4,5], Mohammad Shahrooei[6], Ramanathan Sowdhamini[2], Murali Prakriya[3], Adish Dani[1], Monika Vig[1*]

Address and Affiliation: [1]Tata Institute of Fundamental Research, Hyderabad, India. [2]National Centre for Biological Sciences, Bangalore, India. [3]Northwestern University, Feinberg School of Medicine, Chicago, USA. [4]Institute for Immunodeficiency, University of Freiburg, Germany. [5]Institute for Transfusion Medicine and Gene Therapy, University of Freiburg, Germany. [6]Department of Microbiology, Immunology and Transplantation, Clinical and Diagnostic Immunology, KU Leuven, Leuven, Belgium.

[#, ⊥] These authors contributed equally.

***Correspondence to:** monika.vig@gmail.com

Keywords: Orai, FHLH4, CRAC, Syntaxin11, SOCE, Stim, SNARE, ion channels, autoimmunity, cytotoxicity, CTL, T lymphocytes

Abstract:

Mutations in Syntaxin11, a Q-SNARE, result in a fatal immune disorder known as familial hemophagocytic lymphohistiosis 4 (FHLH4) in human patients. A key diagnostic feature of FHLH4 is defective T and natural killer cell cytotoxicity. Here we show that Syntaxin11 directly binds and regulates Orai1, the pore forming subunit of calcium release activated calcium (CRAC) channels. CRAC channels enable store-operated calcium entry (SOCE) from the extracellular space and are crucial for granule exocytosis and nuclear factor of activated T cells (NFAT) dependent gene expression in activated lymphocytes. Syntaxin11 depletion strongly inhibited SOCE, CRAC currents, NFAT activation, interleukin-2 gene expression and degranulation in FHLH4 patient T lymphocytes and cell lines. Remarkably, defects of granule exocytosis as well as interleukin-2 expression could be reversed by ionomycin induced calcium influx in patient T lymphocytes and a constitutively active, H134S, mutant of Orai1 rescued calcium entry in Syntaxin11 depleted cells. Further mechanistic analyses showed that Syntaxin11 primes Orai1 subunits for correct on-site assembly which is a prerequisite for functional entrapment and gating of CRAC channels by the endoplasmic reticulum resident Stim1. We propose that priming of ion channel pore subunits is a primary and conserved function of specific SNAREs which likely preceded their role in vesicle fusion.

63

64 **Introduction:**

65

66 Familial hemophagocytic lymphohistiocytosis 4 (FHLH4) is a life-threatening
67 immune disease caused due to mutations of STX11 [1]. The underlying cause of FHLH
68 is reduced cytolytic activity of T and NK cells [2], which renders patients susceptible to
69 recurrent infections. Patients suffer from high fever, severe lymphopenia in early infancy
70 and succumb to disease by adolescence, unless given bone marrow transplants. STX11
71 is highly expressed in almost all cells of the immune system and, being a Q-SNARE, is,
72 by default, associated with exocytosis of vesicles. Intriguingly, FHLH4 patients also
73 manifest cytokine storm, which cannot be reconciled with a presumed general defect in
74 membrane trafficking and vesicle fusion.

75

76 Most eukaryotic cells have a limited amount of calcium sequestered inside
77 intracellular stores, the largest of which is the endoplasmic reticulum (ER). Signaling from
78 cell surface receptors induces the release of stored calcium which, in turn, activates store-
79 operated calcium entry (SOCE) to replenish stores, sustain signaling and drive other
80 calcium dependent cellular processes [3]. Calcium release activated calcium (CRAC)
81 channels are the major conductors of SOCE [4]. In lymphocytes and mast cells, CRAC
82 currents have been shown to be crucial for cytotoxicity, degranulation as well as gene
83 expression [5, 6]. Working in concert with a number of accessory proteins, Orai (CRACM)
84 multimers conduct SOCE upon functional clustering with Stim proteins in ER-PM
85 junctions [7-9]. Yet, the prevailing thought attributes all structural transitions that result in
86 the activation of CRAC currents to Stim proteins [10].

87

88 Genome-wide RNAi screens, which initially identified Orai (CRACM), have also
89 yielded a wealth of information regarding additional crucial players in SOCE [8, 11, 12].
90 For instance, we have previously shown that alpha-soluble N-ethylmaleimide sensitive
91 factor (NSF) attachment protein (α-SNAP), a well-known synaptic family adaptor protein
92 that forms a part of the 20S SNARE super-complex [13], is a crucial component of the
93 CRAC channel supramolecular complex [8, 9]. α-SNAP independently binds Stim as well

as Orai and is required for the on-site assembly and calcium selectivity of CRAC channels [14-16]. α-SNAP depletion in cells revealed that Stim:Orai coupling is necessary but not sufficient for SOCE, a process that requires distinct time-resolved molecular steps *in vivo*.

In addition to α-SNAP, some SNAREs also came up as candidates in two genome wide RNAi screens for regulators of SOCE but were not characterized [8, 12]. Furthermore, specific SNAREs have been previously found to form inhibitory associations with some ion channels, but their exact role was not defined [17]. Therefore, we hypothesized a more fundamental function for the association of SNAREs with ion channel pore subunits and set out to test this in the context of SOCE. Using a targeted RNAi screen, biochemical and cell biological analyses, we have found a direct role of STX11 in the correct, on-site, assembly of CRAC channel pore subunit, Orai1, for subsequent gating by Stim1. Analyses of T cells derived from a symptomatic FHLH4 patient showed that the previously reported [2] as well as newly identified defects in degranulation and interleukin-2 gene expression predominantly stem from suppressed SOCE. Based on the findings presented here, we demonstrate a novel SNARE dependent priming step for the CRAC channel pore in the molecular sequence of SOCE and suggest preventive pharmacological interventions for FHLH4 patients.

125 **Results:**

126 RNAi dependent ablation of a Q-SNARE, Syntaxin 5 (STX5), has earlier shown
127 inhibition of SOCE in a genome-wide screen performed in *Drosophila* S2 cells [12] and
128 STX1A has been previously shown to bind a variety of ion channels [17]. Therefore, we
129 first knocked down STX5 (Supplementary Figure 1A) and STX1A (Supplementary Figure
130 1B) using different sequences of shRNA targeting each gene in HEK293 cells and
131 measured SOCE in response to Thapsigargin (TG). In both cases, we did not see a
132 significant defect in SOCE. Since several proteins involved in synaptic function are not
133 ubiquitously expressed and many show redundancy in function, we searched online
134 databases to target SNAREs that are expressed in HEK293 and/or T cells
135 (Supplementary Figure 1C-H). We found that Syntaxin11 knockdown showed strong and
136 consistent inhibition of SOCE by day 4 (Supplementary Figure 2A-B) (Figure 1A-B).
137 Quantitative PCR (qPCR) analysis of total RNA extracted from scramble (scr) and STX11
138 shRNA treated cells showed nearly 70% depletion of STX11 mRNA (Supplementary
139 Figure 2C) and ectopic expression of STX11 in STX11 depleted Jurkat cells rescued
140 SOCE (Figure 1C&D). The efficiency of STX11 depletion was assessed for each
141 experiment reported in this study. We restricted our analysis to day 3 to 4 post RNAi
142 treatment as longer incubations with RNAi or CRISPR knockout of STX11 affected cell
143 viability.

144

145 Given that STX11 is highly expressed in most immune cells and is the only known
146 SNARE that, when mutated, causes defects in T and NK cell cytotoxicity in humans and
147 mice [2], we hypothesized that reduced SOCE contributes to the cytotoxicity defects of
148 FHLH4 patient T cells. To test this hypothesis, we isolated PBMCs from an FHLH4 patient
149 with a homozygous deletion frameshift mutation in the STX11 coding sequence,
150 c.752delA:p.Lys251fs. The patient presented with all symptoms of FHLH4 disease by 4
151 years of age. Given the limited sample amount, we expanded PBMC numbers by
152 periodically stimulating patient and healthy donor cells with PHA and IL-2, prior to
153 analysis. Isolation and Sanger sequencing of DNA from patient PBMCs showed deletion
154 of a single Adenine at position 752 in the STX11 gene which lead to frameshift following
155 Lysine 251 (Figure 1E). The absence of any contaminating wildtype peaks showed that

156 the mutation was present in all blood cells. Figure 1F shows schematic of the predicted
157 mutant STX11 protein with an estimated molecular weight of ~39.5 KDa compared to ~33
158 KDa of wildtype STX11. Frameshift mutation resulted in the disruption of SNARE domain,
159 ablation of the terminal cysteines and elongation of the resulting transcript. We subjected
160 whole cell lysates prepared from the FHLH4 patient and healthy donor (HD) PBMCs to
161 SDS-PAGE and western blot and found that while the wildtype STX11 band was absent,
162 a faint but distinct band running at ~37 KDa was present in the FHLH4 patient sample
163 lysate (Figure 1G and Supplementary Figure 2D). Therefore, the predicted and observed
164 molecular weight of the FHLH4 mutant protein was higher but its levels appeared
165 significantly reduced compared to STX11 from HD. This is likely due to protein instability
166 and degradation because ectopic expression of the FHLH4 mutant in HEK293 cells
167 showed at least two clear bands (Figure 1H and Supplementary Figure 2E), although
168 reduced reactivity to anti-STX11 antibody is also a possibility. In accordance with our
169 findings in the STX11 depleted cell lines (Figure 1A-B and Supplementary Figure 2A-B),
170 SOCE was found to be significantly defective in FHLH4 T cells when compared to HD
171 (Figure 1I). Further, expression of wildtype (Figure 1J), but not FHLH4 mutant STX11
172 (Figure 1K-L), reversed defective SOCE in STX11 deficient patient (Figure 1J) and Jurkat
173 T cells (Figure 1K-L), respectively. These data suggest that FHLH4 mutant STX11 was
174 functionally compromised in addition to being unstable and no additional unknown
175 mutations resulted in reduced SOCE.
176
177 Overexpression of STX1A has been earlier shown to inhibit voltage gated calcium
178 channels (VGCCs) [18, 19]. Since STX11 depletion inhibited SOCE, we next sought to
179 determine the effect of STX11 overexpression. We ectopically expressed STX11 in
180 healthy donor PBMCs (Figure 2A-B), HEK293 and Jurkat T cells (Supplementary Figure
181 3A-B) and measured SOCE. In each of these cases, there was an increase in SOCE,
182 reinforcing a positive role of STX11 in SOCE although ectopic expression of FHLH4
183 STX11 mutant failed to augment SOCE (Supplementary Figure 2F). To determine
184 whether the inhibition in SOCE (Figure 1) and its augmentation (Figure 2A-B) resulted
185 from changes in the activity of CRAC channels, we depleted Orai1 from STX11 over-
186 expressing HEK293 cells, which resulted in complete loss of enhancement observed in

187 SOCE (Figure 2C&D). To quantify the level of Orai1 expression in plasma membrane, we
188 labelled a previously characterized U2OS cell line stably expressing Orai1 tagged with a
189 bungarotoxin binding site (BBS) and YFP (Orai-BBS-YFP) with Alexa-647 conjugated
190 alpha-bungarotoxin (BTX-A647) (Supplementary Figures 3C) [9]. There was no change
191 in the expression of total Orai1 in the PM of STX11 over-expressing (Supplementary
192 Figure 3D) or STX11 depleted cells (Supplementary Figure 3E), even though SOCE was
193 significantly suppressed in these U2OS cells (Supplementary Figures 3F-G). The ER-
194 targeted CEPIA expressing control and STX11 depleted cells showed comparable ER
195 calcium content (Supplementary Figure 3H). Labelling STX11 depleted cells with ER,
196 Golgi organelle specific markers also showed no abnormalities (Supplementary Figures
197 3I&J) suggesting that the overall health, function and calcium content of Golgi and ER
198 were not adversely affected by STX11 depletion.
199
200 Previous studies have shown that SOCE in T cells is mediated by CRAC channels
201 formed by Orai proteins. To test whether CRAC current (I_{CRAC}) was affected by
202 knockdown of STX11 in T cells, we performed whole cell patch clamp recordings on
203 scramble and STX11 shRNA treated Jurkat T cells (Figure 2E-G). Leak-subtracted I_{CRAC}
204 was recorded in 20 mM Ca^{2+} and a Na^{+}-based divalent cation free (DVF) solution. These
205 recordings showed that both the Ca^{2+} and DVF CRAC currents were significantly
206 decreased in the STX11 shRNA treated cells with the normalized currents shown in
207 Figure 2E-G. The electrophysiological properties of the residual current in STX11 shRNA
208 treated cells was indistinguishable from I_{CRAC} in scramble shRNA treated cells in terms of
209 blockade of the Ca^{2+} current by La^{3+} and depotentiation of the DVF current over tens of
210 seconds. Moreover, the reversal potential of the Ca^{2+} and DVF currents were similar
211 between scramble and STX11 shRNA treated Jurkat T cells, suggesting that STX11
212 depletion does not affect the calcium selectivity of CRAC channels (Figure 2H). Together,
213 these results demonstrate that STX11 works by specifically modulating I_{CRAC} in T cells.
214
215 CRAC channel mediated sustained calcium influx is crucial for the activation of a
216 key calcium dependent transcription factor known as nuclear factor of activated T cells
217 (NFAT) [4, 20]. We stimulated control and STX11 depleted Jurkat T cells with

218 Thapsigargin (TG)+PMA, prepared nuclear, cytosolic extracts and subjected them to
219 western blot using anti-NFAT1 antibody (Figure 3A). Nuclear translocation of NFAT was
220 severely compromised in STX11 depleted T cells. In addition, immunofluorescence
221 imaging and quantification of total *versus* nuclear NFAT from anti-CD3 stimulated Jurkat
222 cells showed a defect in nuclear translocation of NFAT1 in STX11 depleted cells (Figure
223 3B-C). To determine whether NFAT induced gene expression was affected [4, 20], we
224 quantified IL-2 mRNA by qPCR and secreted IL-2 levels from culture supernatants of anti-
225 CD3 stimulated Jurkat T cells. STX11 depleted cells showed a significant decrease in IL-
226 2 gene expression as well as secretion (Figure 3D, 3E). We stimulated HD and FHLH4
227 patient T cells either through T cell receptor using anti-CD3 or with phorbol myristate
228 acetate (PMA) + Ionomycin and assessed IL-2 gene expression. Importantly, induction of
229 IL-2 expression was significantly defective in FHLH4 patient T cells but could be largely
230 restored with Ionomycin (Figure 3F). We next performed granule release assay on the *in*
231 *vitro* cultured HD and FHLH4 patient CD8 T cells in response to anti-CD3 mediated
232 stimulation and observed a significant defect in the FHLH4 patient CD8 T cell
233 degranulation (Figure 3G, 3H). To determine whether the reduced granule release results
234 from a direct defect in vesicle fusion or SOCE, we stimulated cells with Ionomycin along
235 with (PMA). Remarkably, CD8 T cell degranulation was fully restored in FHLH4 T cells
236 suggesting that defective SOCE primarily causes cytolytic defects in FHLH4 T cells. Of
237 note, the patient exhibited all symptoms of FHLH by 4 years of age and we observed
238 strong suppression of SOCE (Figure 1I), IL-2 gene expression and secretion (Figure 3D-
239 F). However, *in vitro* culture of FHLH4 patient CD8 T cells with IL-2 has been previously
240 shown to partially or fully restore cytolytic defects by other groups [21, 22]. Therefore,
241 considering previous reports, a relatively lower (50%) defect in CD8 T cells degranulation
242 was not surprising [21, 22]. Collectively, these data suggest that defects in T cell
243 degranulation as well as interleukin-2 gene expression originate from suppressed SOCE
244 and significantly contribute to the immune dysregulation of FHLH4 patients.
245
246 Unlike most Q-SNAREs, STX11 lacks a transmembrane domain but harbors a
247 stretch of cysteines close to the C-terminus (Supplementary Figure 4A), which have been
248 proposed to be essential for its membrane localization [23]. The cellular localization of

249 STX11 is not established primarily because, unlike primary T cells, native STX11 is
250 undetectable in Jurkat and HEK293 cell lines using available commercial antibodies and
251 tagging STX11 on either N- or C-terminus result in partial degradation (Supplementary
252 Figure 4B) and complete mis-localization of the protein (Supplementary Figure 4C).
253 Therefore, we inserted HA tag inside the N-terminal unstructured region of STX11,
254 expressed in HEK cells, permeabilized and labelled with anti-HA tag antibody. The HA
255 tagged human STX11 localized in the plasma membrane (Supplementary Figure 4D). We
256 next expressed untagged human STX11 in cells co-expressing Orai1-YFP, permeabilized
257 and stained with anti-STX11 antibody. In most cells, STX11 co-localized with Orai1 in
258 plasma membrane (Figure 4A). To test whether STX11 and Orai1 formed a complex, we
259 co-expressed STX11 with either Flag- or Myc-tagged Orai1 in HEK293, prepared whole
260 cell lysates (WCLs) and subjected them to co-immunoprecipitation (co-IP) followed by
261 western blot using either anti-Flag, anti-Myc or anti-STX11 antibodies. Both Orai1 and
262 STX11 could co-IP each other (Figure 4B-C) (Supplementary Figure 5A-B). To further
263 assess whether STX11 directly bound Orai1, we expressed and purified from *E. coli*,
264 MBP-tagged N- and C-terminal cytosolic tails of Orai1 (Figure 4D). *In vitro* pull-down
265 assay performed by incubating MBP-tagged Orai1 cytoplasmic tails with full length
266 soluble His-tagged STX11 showed that the C-terminus of Orai1 directly bound STX11
267 (Figure 4E) (Supplementary Figure 5C). SNAREs typically utilize their SNARE domain for
268 associating with other SNAREs [24]. To identify the domain of STX11 involved in the
269 regulation of SOCE, we expressed His-tagged H_{abc} and SNARE domains of STX11 in *E.*
270 *coli*, purified and assessed their binding to the MBP-tagged Orai1 tails using pull-down
271 assay. We found that the H_{abc} domain of STX11 bound to the C-terminus of Orai1 (Figure
272 4F) (Supplementary Figure 5D). The SNARE domain did not show any binding to Orai1
273 and only a faint binding to SNAP23 (Supplementary Figure 5E). We next used AlphaFold3
274 (AF3) to obtain deeper insights into the domain-domain interactions of STX11 and Orai1.
275 Of all the possible combinations, the complex of STX11 H_{abc} and Orai1 C-terminus
276 resulted in a significantly high prediction score (Supplementary Table 1). We, therefore,
277 executed AF3 predictions with different initial seeds to generate multiple models of STX11
278 H_{abc} with Orai1 C-terminus. We calculated the contact frequency of interface residues in
279 different models and found that multiple residues showed frequency greater than 0.8

280 (Supplementary Figure 6). For further analysis, we considered the predicted model with
281 the best score (Supplementary Table 2). Next, we performed all-atom MD simulation in
282 aqueous environment (Movies 1-3) to assess the conformation, interaction stability of the
283 STX11 H_{abc} and Orai1 C-terminus complex, which was stable throughout the simulation
284 time as assessed through RMSD (Supplementary Figure 7), and binding free energy (ΔG)
285 (Supplementary Figure 8A) (Figure 4G). The individual trajectories were concatenated
286 and clustered to obtain a centroid structure for this complex. There were 46 clusters, and
287 the largest cluster, with 52 members, showed an elaborate protein-protein interface where
288 STX11 H_{abc} was found to be oriented in an anti-parallel orientation to Orai1 C-terminus
289 (Figure 4H).
290
291 Because STX11 binds the C-terminus of Orai1 and the region largely overlaps with
292 Stim1 binding domain, we next sought to determine whether STX11 co-localizes with
293 Orai:Stim puncta. We over-expressed untagged STX11 in a Orai1-YFP and CFP-Stim1
294 expressing stable HEK293 cell line, store-depleted with TG and stained using anti-STX11
295 antibody. We did not observe STX11 in Orai:Stim puncta (Figure 4I). Accordingly, STX11
296 did not co-IP with Stim1 (Supplementary Figure 9A). These data suggest that STX11
297 comes off Orai1 C-terminus prior to Stim1 dependent clustering of Orai1. Since co-IP
298 studies suggested sustained interaction between STX11 with Orai1 (Figure 4B-C), we
299 quantified the fraction of Orai1 in Stim:Orai puncta w.r.t total Orai1 in PM and found that
300 nearly 60% Orai1 remains outside of Stim1 puncta in unmanipulated cells, even 8 minutes
301 post TG addition (Supplementary Figure 9B). We next performed all-atom MD simulations
302 on Orai1 C-terminus (256-301) and the Orai activation domain of human Stim1 (312-387),
303 previously studied in an NMR study [25] (Supplementary Figure 9C). We used AF3 to
304 generate the complex of Stim1 and Orai1. The single copy as well as two copies of Stim1
305 with monomeric Orai1 resulted in low prediction scores (Supplementary Table 3-4).
306 Nonetheless, ΔG values between the protomers of Stim1 and Orai1 (Figure 4J)
307 (Supplementary Figure 9D) were comparable to that of STX11 and Orai1 (Figure 4G).
308 We next used two copies each of Stim1 and Orai1 to generate the complex. The best
309 scoring model among multiple runs of AF3 (Supplementary Table 5), was considered for
310 the MD simulation. Three independent MD simulations were run for the Stim1:Orai1

311 tetramer (Movies 4-6). The Stim1:Orai1 complex showed initial large conformational
312 change but stabilized thereafter (RMSD, Supplementary Figure 10A). The ∆G values for
313 dimers of Stim1 and Orai1 remained stable throughout the simulation period and were
314 found to be significantly more negative compared to STX11:Orai complex and Stim:Orai
315 protomers (Supplementary Figure 10B) (Figure 4K). All three simulation trajectories were
316 concatenated and clustered to obtain a centroid structure for this complex
317 (Supplementary Figure 10C). There were 47 clusters, and the largest cluster had 63
318 structures. Collectively, these data suggest that STX11 directly binds Orai1 with affinities
319 similar to that of Stim1:Orai1 protomers. However, presence of higher density of Stim1 in
320 ER-PM junctions of store-depleted cells could, in theory, outcompete STX11:Orai1
321 interactions by progressively allowing formation of Stim1:Orai1 dimers/ oligomers.
322
323 The major interactions predicted between STX11 and Orai1 from all-atom MD
324 simulations are highlighted in (Supplementary Figure 8B-C). To assess the significance
325 of predicted interactions, we performed site-directed mutagenesis of two key residues of
326 STX11 predicted to be involved in binding to Orai1 (Figure 5A). Ectopic expression of
327 untagged N147A_E150A STX11 showed correct localization (Figure 5A) as well as stable
328 expression (Figure 5B) (Supplementary Figure 11A) but failed to rescue SOCE in STX11
329 depleted Jurkat T cells (Figure 5C-D). We next expressed His-tagged wildtype and
330 N147A_E150A mutant STX11 in *E. coli.*, purified (Figure 5E) and assessed their ability to
331 bind MBP-tagged Orai1 C-terminal tail in an *in vitro* pull-down assay (Figure 5F)
332 (Supplementary Figure 11B). Compared to wildtype STX11, N147A_E150A mutant
333 STX11 showed reduced binding to Orai1 C-terminus. Further, we introduced four
334 mutations, R289A_E272A_E275A_E278A, in the Orai1 C-terminus (Figure 5G), tagged
335 with YFP and expressed in HEK293 cells. The Orai1 mutant localized to PM (Figure 5G)
336 but failed to rescue SOCE in Orai1 deficient cells (Figure 5H-I). We expressed and
337 purified MBP-tagged R289A_E272A_E275A_E278A mutant Orai1 C-terminus from *E.*
338 *coli* and assessed its ability to bind purified wildtype as well as N147A_E150A mutant
339 STX11 in a pull-down assay (Figure 5J) (Supplementary Figure 11C). Binding of Orai1
340 mutant to both was significantly compromised. Because Stim1 binds an overlapping
341 region of Orai1 C-terminus, we next tested whether mutation of Orai1 residues affected

342 Stim1 binding. We co-expressed YFP-tagged soluble CRAC activation domain (CAD) of
343 Stim1 (YFP-CAD) (Figure 5K) with either CFP-tagged wildtype or mutant Orai1 in
344 HEK293 cell line. YFP-CAD localizes to the cytosol in HEK293 cells but in cells
345 overexpressing Orai1, a significant fraction of it localizes to plasma membrane due to its
346 association with Orai1 [10]. We quantified relative YFP-CAD levels in the plasma
347 membrane of both groups (Figure 5K-L) but found no difference in PM recruitment of CAD
348 suggesting that the inability of R289A_E272A_E275A_E278A mutant Orai1 to support
349 SOCE does not result from defective binding to Stim1. Collectively, these data
350 demonstrate a direct role of STX11 in the binding and regulation of Orai1.
351
352 Upon store depletion, Stim1 localizes to ER-PM junctional regions where it traps
353 and co-clusters with Orai1. To further understand the mechanism, we first imaged
354 HEK293 cells expressing CFP-Orai1, Stim1-YFP under resting conditions and then
355 quantified the levels of Orai1 and Stim1 in ER-PM junctions (puncta) of store-depleted
356 control and STX11 depleted cells. The distribution of Orai1 and Stim1 was normal in
357 resting cells (Figure 6A). However, in store-depleted cells, clustering of CFP-Orai1 was
358 visibly defective in STX11 RNAi treated cells (Figure 6B), even though the intensities
359 (Figure 6C) and area of Stim1-YFP puncta were normal (Figure 6D). Quantification of
360 Orai1 intensities confirmed a significant defect in entrapment (Figure 6E) with relatively
361 higher fraction of Orai1 present outside Stim1 puncta in STX11 depleted cells (Figure 6F).
362 To determine whether reduced Orai1 clustering resulted from structural defects within
363 ER-PM junctions, we reversed the direction of fluorescent tags on Orai1 as well as Stim1
364 and repeated the experiment in Figure 6A-F. Interestingly, the defect in Stim1 mediated
365 entrapment of Orai could be rescued (Supplementary Figure 12A-B) (Figure 6G-J) but
366 SOCE remained significantly inhibited even when Orai and Stim were co-overexpressed
367 (Figure 6K-L). Taken together, these data show that STX11 binding to resting Orai1 has
368 implications beyond mere co-entrapment of Orai1 with Stim1 and STX11 depletion does
369 not alter the structure or proximity of junctional ER to the PM. Importantly, STX11 was
370 found to be limiting in cells co-overexpressing Orai and Stim that have been proposed to
371 be sufficient for amplifying CRAC currents in earlier studies using patch clamp [26] [27]
372 [28].

373 Defects in the entrapment of Orai1 suggest absence of a necessary molecular
374 transition within Orai1 which precedes its interaction with Stim1. Using step
375 photobleaching, we have previously shown that under resting conditions, Orai1 exists as
376 a dimer but forms higher order oligomers, on-site, upon store-depletion [14] [29]. To
377 directly test whether SNAREs contributed to the on-site assembly of CRAC channel pore
378 subunit, we co-expressed Orai1-CFP along with Orai1-YFP in control or STX11 depleted
379 HEK293 cells and measured Orai:Orai FRET. Remarkably, we found significantly higher
380 Orai:Orai FRET in STX11 depleted cells even in the absence of Stim1 or store-depletion
381 (Figure 7A). We then sought to determine whether store-depletion could induce a similar
382 transition in Orai1 in absence of Stim1 in store-depleted scramble control cells. Indeed,
383 we found Orai:Orai FRET to be significantly higher post store-depletion when compared
384 to resting state control cells (Figure 7B). In STX11 depleted cells, however, store-
385 depletion did not show any further increase in FRET over and above what was already
386 observed in resting cells.
387
388 Increasing the density of Stim1 has been earlier proposed to bypass the
389 requirements for accessory factors in SOCE. To determine whether increasing the levels
390 of Stim1 could compensate for STX11 depletion, we expressed Orai1 tethered to two
391 Stim-Orai activating regions (SOAR) of Stim1 and GFP (Orai1-S-S-GFP) (Supplementary
392 Figure 13A-B) in HEK293 cells. Orai1-S-S-GFP has been previously shown to
393 constitutively activate Orai1 [30]. In STX11-depleted Orai1-S-S-GFP expressing cells, the
394 magnitude of calcium entry was significantly smaller (Supplementary Figure 13C-D). To
395 determine whether reduced calcium entry resulted from a defect in the ability of SOAR to
396 bind Orai1, we expressed YFP-CAD (Supplementary Figure 13E), in control or STX11
397 depleted Orai1-CFP expressing HEK293 cell line. Quantification of PM localized YFP-
398 CAD as a fraction of total CAD showed no defect in STX11 depleted cells (Supplementary
399 Figure 13E-F). Yet, as seen with Orai1-S-S-GFP, constitutive calcium entry was
400 significantly reduced (Figure 7C-E). We next expressed the constitutively active H134S
401 mutant of Orai1 (Supplementary Figure 13G) as it harbors an open pore and the C-
402 terminal cytosolic tails of Orai1 are unlatched, pointing towards the cytosol [31].
403 Remarkably, expression of H134S Orai1 completely restored constitutive calcium influx

404 in STX11 depleted cells (Figure 7F-G). To further determine whether binding with STX11
405 induces straightening of Orai1 tails or molecular transitions within transmembrane
406 helices, we expressed in STX11 depleted cells the constitutively active ANSGA (261-265)
407 mutant of Orai1 (Supplementary Figure 13H), which harbors 4 consecutive mutations in
408 the Orai1 C-terminus resulting in the constitutive activation of CRAC currents along with
409 straightening of the C-terminal tail [32]. Intriguingly, constitutive calcium entry in STX11
410 deficient, Orai1 ANSGA mutant expressing cells was significantly suppressed (Figure 7H-
411 I). Taken together, these data show that STX11 induces a molecular switch in the pore-
412 forming subunit of CRAC channels, which precedes and primes Orai1 for correct
413 assembly and successful gating by Stim1. Such SNARE dependent priming of Orai1 is
414 crucial and cannot be compensated by merely increasing the density of Stim proteins
415 bound to Orai or by introducing mutations that alter the orientation of Orai1 tails *in vivo*.
416 A hypothetical model depicting unprimed and primed Orai1 is shown in Figure 7J.
417
418 Q-SNAREs are often found in complex with other SNAREs such as SNAP23/25/29
419 in target membranes. Some previous studies have implicated the complex of SNAP23/25
420 and STX1A in the regulation of specific ion channels [33, 34]. The three SNAPs,
421 SNAP23/SNAP25/SNAP29 are each capable of contributing two SNARE domains to the
422 *trans*- and *cis*-SNARE complex. RNAi mediated depletion of SNAP23/SNAP25/SNAP29
423 did not show a significant reduction in SOCE (Supplementary Figure 14A-C). To
424 determine whether SNAP23/SNAP25/SNAP29 might still form a part of the STX11:Orai
425 complex to regulate SOCE, we co-expressed myc-tagged Orai1 with untagged SNAPs
426 and performed respective co-IPs. We did not find any interaction between either of the
427 three SNAPs and Orai1 (Supplementary Figure 14D). Similar studies were performed by
428 co-expressing YFP-Stim1 and the three myc-tagged SNAPs. Again, no interaction was
429 found between any of the SNAPs and Stim1 (Supplementary Figure 14E). These data
430 show that unlike in the case of vesicle fusion, STX11 does not collaborate with
431 SNAP23/SNAP25/SNAP29 in the regulation of SOCE.
432
433 FHLH is a heterogeneous immune disorder where diverse genes such as *STX11*,
434 *UNC13D*, *Prf1*, *Munc18-2*, *MAGT1, XIAP, LYST, AP3B1, RAB27A*, *ITK*, amongst several

435 others, are broadly grouped together based on disease symptoms, although the age of
436 onset and severity varies across the spectrum [35, 36]. Congenital immunodeficiency
437 involving defects in the CTL and NK cell cytotoxicity appear to be the common factors
438 underlying the development of FHLH, although the individual pathways involved are
439 highly diverse. Using shRNA, we screened 6 additional genes, *Perforin1*, *RAB27A*,
440 *UNC13D* and *Munc18-2*, *Synaptotagmin11* and *13*, that have been either associated with
441 vesicle fusion or routinely grouped together with STX11 in diagnosing FHLH
442 (Supplementary Figure 15). SOCE was not affected by depletion of most genes. Future
443 studies will evaluate the role of others.
444
445
446 **Discussion:**
447
448 CRAC channels conduct a small but highly calcium specific current in response to
449 the depletion of intracellular calcium stores. According to the prevailing view, preformed
450 Orai hexamers reside in the PM and depend on the ER resident store sensor Stim for all
451 structural transitions leading up to their activation [10]. Unlike other ion channels, the
452 process of activation of CRAC currents is exceptionally slow. For instance, following
453 break-in or store-depletion, on average, it takes ~5 minutes for Stims to cluster in the ER-
454 PM junctions and for measurable CRAC currents to flow from Orai. During this time, Stim
455 proteins undergo intramolecular transitions and slowly trap and gate freely diffusing Orai.
456 It is therefore believed that no molecular transitions take place within the pore forming
457 subunit, Orai, until its clustering by Stim in the ER-PM junctions.
458
459 In STX11 depleted cells, despite normal distribution of resting and store-depleted
460 Stim1, the clustering of CFP-Orai1, which is thought to be entirely dependent on
461 associations with Stim1, was visibly defective (Figure 6B-F). Given that Orai:Orai FRET
462 was defective in STX11 deficient cells even in the absence of Stim1 and store-depletion,
463 we have shown that Orai1 undergoes, a hitherto unrecognized, SNARE dependent early
464 molecular transition which precedes clustering and gating by Stim1. Given our earlier
465 findings of variable Orai1 stoichiometry in resting *versus* store-depleted cells [14], the

466 most likely explanation for ~25% increase over basal Orai:Orai FRET upon STX11
467 depletion or store-depletion is oligomerization of Orai1 dimers into higher order oligomers.
468 A mere 5% increase in absolute NFRET values, for instance, can indicate up to 10-fold
469 increase in interaction.
470
471 Stim1 binds both the N- as well as the C-terminus of Orai1 but their individual
472 relevance in the trapping *versus* gating of Orai1 remains unclear [37]. Switching the large
473 fluorescent tag from the Orai1 N- to the C-terminus could rescue its clustering but not
474 gating by Stim1, essentially reinforcing the idea that STX11 induced molecular shifts in
475 Orai1 do not merely correct orientations of cytosolic tails for trapping. Orai cytosolic tails
476 have been shown to be crucial for CRAC channel gating but are missing from the
477 structures of *Drosophila* Orai [31]. A previous NMR structure suggested that C-terminal
478 tails of two adjacent Orai1 subunits, bend, pair with each other in an antiparallel fashion
479 and sit closely apposed to PM [25]. However, in structures of constitutively active H134
480 mutant Orai, the C-terminal tails were found to orient away from plasma membrane [31].
481 We have shown that the ANSGA mutant of Orai1 [32], but not H134S Orai1, was sensitive
482 to STX11 depletion. These data agree with FRET and suggest that STX11 facilitated
483 molecular transitions occur within the transmembrane regions of Orai1 rather than
484 changing the orientations of Orai1 tails. The changes in resting cell Orai:Orai FRET
485 showed that such transition precedes the association and clustering of Orai with Stims.
486 These data align with our findings of an overlapping region of Orai1 bound by STX11 and
487 Stim1. Because tagging of STX11 on either end with fluorescent tags results in mis
488 localization and degradation, our study could not demonstrate the real-time removal of
489 STX11 from the Orai1- C-terminus to allow for Stim1 binding in live cells. It is also unclear
490 whether binding or removal of STX11 induces the correct transition in Orai1 assembly.
491 Further, it remains to be determined whether STX11 removal is actively induced by an
492 additional chaperone or passive competition due to formation of relatively higher affinity
493 dimeric/oligomeric associations between Orai1:Stim1 in ER-PM junctions (Figure 4K).
494 Future studies will be able to systematically evaluate each of these possibilities.
495

496 We have shown that the C-terminal cytosolic tail of Orai1 directly couples with
497 STX11 in resting cells (Figure 4). Although binding appeared reasonably strong in co-
498 IPs, STX11:Orai1 interaction appeared relatively weak in pull-downs (Figure 4). This is
499 likely due, in part, to the instability of purified His-STX11 in solution which necessitated
500 shorter co-incubation times during pull-down assays. Instability could arise from the
501 absence of a co-chaperone, such as one of the known binding partners of the synaptic
502 family or membranes to which STX11 attaches in lives cells *via* its C-terminal cysteines
503 [23]. Together, these factors could be crucial for the stabilization of purified STX11 *in vitro*.
504
505 Previous whole cell patch clamp analysis of HEK293 cells co-overexpressing Orai1
506 and Stim1 has shown up to 50-100-fold amplification of CRAC currents whereas Fura-2
507 based live imaging of the same cells routinely shows only 2-fold amplification [26] [27]
508 [28]. The difference in the fold change between these two readouts is often used to
509 extrapolate and conclude that all other accessory factors that have since been identified
510 are either not limiting or unnecessary for native CRAC currents. A major problem with this
511 interpretation is that even though amplification of CRAC currents was shown, none of the
512 previous patch clamp studies established whether the higher currents resulted from a
513 greater number of active channels or unchecked conductance per channel by performing
514 single channel recordings. The fact that recording of I_{CRAC} in the whole cell configuration
515 involves dialysis of cells with high concentrations of BAPTA, a fast calcium chelator, the
516 calcium dependent inactivation of CRAC channels, a key mechanism of regulation of
517 I_{CRAC} amplitude in live cells is disrupted. Furthermore, BAPTA mediated chelation of Ca^{2+}
518 ions and voltage clamping at hyperpolarizing potentials to record amplified CRAC
519 currents prevents the progressive depolarization of cells due to influx of positively charged
520 ions which would have otherwise dampened the driving force for CRAC currents in intact
521 cells. Given these limitations, Fura-2 assays offer a more physiological reflection of SOCE
522 amplitudes in live cells as they allow for these regulatory mechanisms, which are
523 necessary for the regulation of native currents to be still operational in live cells. While
524 patch clamp remains a direct method of verification of CRAC currents, exercising logic
525 and caution in interpreting amplitudes of I_{CRAC} is imperative in order for the field to move
526 forward. Using Fura-2 imaging assays in STX11 depleted cells, we have conclusively

527 established that STX11 is necessary as well as limiting not only in live and unperturbed
528 HEK, U2OS, Jurkat and primary T cells but also HEK293 cells co-overexpressing Orai1
529 and Stim1 (Figure 6K-L).
530
531 Most human mutations in the *STX11* coding region result in the complete loss or
532 severe depletion of STX11 protein levels [23]. The FHLH4 disease, therefore, results from
533 reduced STX11 expression in most reported patients. Targeted mutagenesis of the
534 STX11:Orai1 interface lining residues based on the AlphaFold 3 model, however, didn't
535 destabilize or mis-localize either N147A_E150A STX11 or
536 R289A_E272A_E275A_E278A Orai1 and yet both mutants showed reduced binding to
537 their respective wildtype counterparts. Importantly, the R289A_E272A_E275A_E278A
538 mutant of Orai1 retained the ability to bind Stim1.
539
540 In addition to the established cytolytic defects in FHLH4 T cells, for the first time,
541 we have shown that STX11 deficient and FHLH4 T cells harbor a severe defect in SOCE,
542 NFAT signaling, IL-2 cytokine expression and secretion. Therefore, our data strongly
543 suggest that T cell calcium signaling defects significantly contribute to FHLH4 disease
544 progression, independent of exocytotic defects. We propose that design and early
545 administration of CRAC channel agonists could potentially provide an alternative to
546 immunosuppressants and bone marrow transplants for FHLH4 patients.
547
548 In summary, we have shown that binding to a Q-SNARE, STX11, provides an on-
549 site molecular switch in the CRAC channel pore, Orai1, necessary for its correct
550 assembly, functional coupling and gating by Stim1. We suggest that ion channel priming
551 is a novel, direct and primary role of specific SNAREs. In accordance with this hypothesis,
552 early SNARE-like proteins have been found in bacteria, which lack an endomembrane
553 system but express a variety of ion channels [38-40]. SNAREs are now thought to have
554 evolved from a common archaeal precursor found in the genomes of Asgard and
555 members of *Legionella* [41].
556
557

558 **Materials and Methods**

559

560 **Plasmid constructs and transfection**

561 Stim1 CAD was sub-cloned in eYFPC1 vector after amplification from YFP-Stim1 plasmid
562 to generate YFP-CAD. pLKO.1, psPAX2 and pMD2.G were purchased from Addgene.
563 pLKO.1 cloned shRNA sequences targeting the genes of interest, were either purchased
564 from Horizon Discovery, UK or designed and cloned in-house using the Broad Institute
565 portal (https://portals.broadinstitute.org/gpp/public/gene/search). Full-length human
566 STX11 was cloned from human cDNA prepared from HEK293 cells and subcloned into
567 pcDNA3.1(+), pcDNA/4TO/Myc-HisA (Invitrogen, Grand Island, NY), pMSCV-IRES-
568 mcherry (Addgene), pEF1alpha-IRES (Clontech) and pET28b vector [16] with an N-
569 terminal 6XHis-tag. The fragments of STX11 were cloned in pET28b vector with an N-
570 terminal 6xHis tag for expression in *E. coli*. HA tag was inserted between H30 and G31
571 in STX11 cloned in pMSCV-IRES-mCherry construct using PCR. H134S and ANSGA
572 mutants of Orai1 were generated using site directed mutagenesis and PCR, respectively.
573 The fragments of Orai1 (1-87, 1-47, 48-103, 256-301 and 272-292) were amplified from
574 full length constructs and cloned into pMAL-c5X vector (New England Biolabs), in-frame
575 with MBP protein coding sequence, as described previously [16]. SNAP23, SNAP25 and
576 SNAP29 cDNA cloned in pCMV-Sport6.1 vectors were purchased from Dharmacon and
577 subcloned into pcDNA4/TO/Myc-HisA. SNAP23 was subcloned in pMAL-c5X vector in-
578 frame with MBP. All plasmid DNA transfections in human cell lines and primary cells were
579 done using Lipofectamine 2000 (Invitrogen)/ Lipofectamine 3000 (Invitrogen) or Amaxa
580 nucleofection kit (Lonza, Basel, Switzerland) respectively, as per manufacturer's protocol.

581

582 **Cell Lines**

583 Lentiviral shRNA transduction experiments were performed in HEK293, U2OS or Jurkat
584 (ATCC, Manassas, VA) cell lines cultured in low glucose DMEM (Hyclone, Logan, UT) or
585 RPMI (Hyclone) respectively, with 5-10% fetal bovine serum (Hyclone), 1X Penicillin
586 Streptomycin, and GlutaMax (Gibco, Grand Island, NY). Stable cell lines generated using
587 HEK293 and U2OS parent lines have been described previously [9]. HEK293-FT cell line
588 was cultured in high glucose DMEM with 10% FBS and 10mM HEPES, 1X Penicillin

589 Streptomycin, 1X GlutaMax and 1X non-essential amino acid and transfected with the
590 appropriate plasmids to generate viral supernatants. All cell lines were tested for
591 mycoplasma contamination twice every year and found to be negative.
592
593 **Antibodies and Reagents**

Antibodies/Reagents	**Source and Cat no**	**Dilution/ Conc.**
Mouse anti-myc (9E10)	Abcam #ab32	1:1000
Mouse anti-myc (9E10)	Culture supernatant, in house	1:1000
Rabbit anti-SNAP23	SYSY#111203	1:1500
Mouse anti-SNAP25	SYSY#111011	1:1500
Rabbit anti-SNAP29	SYSY#111303	1:1500
Rabbit anti-GFP	Invitrogen#A11122	1:2500
Rabbit anti-flag	Sigma#F7425	1:1600
Mouse anti-flag (M2)	Sigma#F3165	1:1500
Mouse anti-6X His	Invitrogen #MA1-135	1:2000
Rabbit anti-Stx11	Sigma#SAB4301593	1:1000
Mouse anti-NFATc2 (4G6-G5)	Santacruz#7296	1:500
Rabbit anti-NFAT1	Cell Signaling Technology #4389	1:200
Goat anti-Lamin B (M-20)	Santacruz#6217	1:500
Rabbit monoclonal anti-HA	CST#3724S	1:1000
Alpaca VHH anti-rabbit AF488	Jackson #611-544-152	1:400 (1.375μg/ml)
DAPI	Invitrogen #D1306	2μg/ml
Rabbit anti-Stx11	SySy #110113	1.67μg/ml
Rabbit anti-Stx11	Invitrogen #PA5-50800	1:2000
Goat anti-rabbit A647	Invitrogen #A-21245	1:800
Rabbit anti-Stx11	Proteintech #13301-1-AP	0.3μg/ml
Donkey anti-rabbit A647	Jackson #711-605-152	1:800

HRP GAPDH	Sigma #G9295	1:40000
HRP Donkey anti-Rabbit	Jackson #711-035-152	1:50000
HRP Donkey anti-Mouse	Jackson #715-035-151	1:50000
Purified Human IL-2	BD #555051	1 μg/ml
Purified Human IL-2 Biotin	BD #555040	1 μg/ml
Streptavidin HRP antibody	Jackson #016-030-084	0.1 μg/ml
Ultra-LEAF Purified anti-human CD3	Biolegend #317326	5-10μg/ml
Ultra-LEAF Purified anti-human CD28	Biolegend #302934	2μg/ml
Ultra-LEAF Purified anti-human CD49d	Biolegend #304340	2μg/ml
PE anti-human CD107a (LAMP-1)	Biolegend #328608	1:50
APC anti-human CD8 antibody	Biolegend #344722	0.5μg/ml
Fura-2-AM	Invitrogen #F1221	1μM
Thapsigargin (TG)	Sigma #T9033-1MG	1μM
Polybrene (Hexadimethrine-bromide)	Sigma #107689-10G	8μg/ml
NE-PER kit	Thermo #78833	
Protein A/G Mag Sepharose xtra	Cytiva #28967056/66	
Protein A/G 4 Fast Flow Sepharose	Cytiva #17528001	
Protease Inhibitor Cocktail (Mammalian)	Sigma #539134	
Protease Inhibitor Cocktail (Bacterial)	Calbiochem #539132	
Talon Beads	Takara #635502	
Dextrin Sepharose Beads	Cytiva #28935597	

HEPES	Sigma #H3375-100G	
Lipofectamine 2000	Thermofisher #11668019	
Lipofectamine 3000	Thermofisher #L3000001	
Lemo21(DE3) *E.coli.* cells	NEB #C2528J	
IPTG	Himedia#MB072-10G Sigma #16758-10G	
Sarkosyl (N-lauroylsarcosine sodium salt)	Sigma #L9150-50G	
Lysozyme	Sigma #62970-5G-F	
DNaseI Recombinant RNase-free	Roche #04716728001	
PMA (Phorbol Myristate Acetate)	Sigma #P8139	20-50ng/ml
Ionomycin	Sigma #407952	1μM
Human IL-2 protein	Acro Biosystems #H5215	50ng/ml
Lectin from *Phaseolus vulgaris* (PHA)	Sigma #L8754	2μg/ml
Retronectin	Takara #T100B	20μg/ml
RNeasy Plus Mini kit	Qiagen#74134	
QIAshredder	Qiagen#79654	
Superscript IV	ThermoFisher#18091300	
Qubit ssDNA Assay kit	ThermoFisher# Q10212	
Human STX11 TaqMan probe (FAM-MGB)	ThermoFisher# Hs00186823_m1	
Human Beta Actin TaqMan probe(FAM-MGB)	ThermoFisher# Hs01060665_g1	
Human IL2 Taqman probe (FAM-MGB)	ThermoFisher# Hs00174114_m1	
Paraformaldehyde	Electron Microscopy Sciences #157-8	

Bovine Serum Albumin	Jackson #001000173	
Luria Bertini Broth	Himedia #M1245	
HBSS	Sigma #H8264	
Terrific Broth	Sigma #T9179	
Alexa fluor 647 conjugated Alpha Bungarotoxin	Invitrogen #B35450	1μg/ml
HRP rabbit anti-GFP	Invitrogen #A10260	
HRP Goat anti-rabbit Fc	Jackson #111-035-008	1:50,000
Ampicillin	Sigma #A0166-5G	100ug/ml
Kanamycin	Sigma #K1876-1G	50ug/ml
Chloramphenicol	Sigma #C 0378-5G	100ug/ml
30% Acrylamide:Bis Solution (29:1)	Biorad #1610156	
DTT (Dithiothreitol)	Biorad #1610611	
0.05% Trypsin-EDTA	Gibco #25300054	
100X Penicillin Streptomycin	Sigma #P4333-100ML	
Puromycin	Gibco #A11138-03	
Pluronic F-127 (20% solution in DMSO)	Invitrogen #P3000MP	0.02%

Lentiviral transductions

For the generation of lentiviral supernatants, shRNAs cloned in pLKO.1 were co-transfected with psPAX2 packaging and pMD2.G envelope plasmids into HEK293-FT cells using the calcium phosphate method of transfection. 48- and 72-hours post-transfection, viral supernatants were collected, pooled and stored at -80°C till further use. For transduction of HEK293 and Jurkat cells, 0.1 million cells were plated in 6- or 24-well plates either the day before (HEK293) or the same day (Jurkat). Viral supernatants were added to the cells along with 8ug/ml polybrene and cells were spun at 2500 RPM, 30°C for 90 mins. 24 hours or 48 hours post-spinfection, Puromycin was added at a final

606 concentration of 1ug/ml to HEK293 and Jurkat cells, respectively. Cells were analyzed 3-
607 5 days post transduction.
608
609 **Immunocytochemistry and confocal imaging**
610 For STX11 localization, resting or store-depleted (1μM Thapsigargin) WT HEK293 or
611 HEK293 cells stably expressing Orai1-YFP were either plated in 6 well plates and
612 spinfected with viral supernatants generated from pMSCV-STX11(HA)-IRES-mCherry,
613 pMSCV-IRES-mCherry (empty vector control) or plated in carbon coated, glow
614 discharged 35mm glass bottom dishes (IBDI) and transfected with pEF1alpha-STX11-
615 IRES-mCherry. 24 hr post-spinfection, cells were plated in 35mm glass bottom dishes.
616 For immunolabelling, cells were washed with Ringer's buffer, fixed with 4% PFA and
617 blocked with 3% BSA containing 0.1% NP40 for 1.5 hrs. Post-fixation and
618 permeabilization, cells were incubated either with anti-HA (CST) or rabbit anti-Stx11
619 (SySy/ Proteintech) primary antibodies O/N at 4°C, washed and incubated with either
620 Alpaca VHH anti-rabbit AF488, donkey anti-rabbit A647 or goat anti-rabbit A647
621 secondary antibodies for 1 hour at room temperature (RT). Cells were counter stained
622 with DAPI for 10 min at RT and imaged using Olympus FV3000 laser scanning confocal
623 microscope. Images were acquired sequentially using the following parameters: DAPI
624 (DM405/488 dichroic, 405nm excitation, 430-470nm emission); anti-HA Alexa488
625 (DM405/488, 488nm excitation, 500-590nm emission); STX11 (DM405/488/561/640,
626 640nm excitation, 650-750nm emission); Orai1-YFP (DM405/488/561/640, 488nm
627 excitation, 521-591nm emission); CFP-Stim1 (DM405-445/514/594, 405nm excitation,
628 448-510nm emission). For STX11-N147A-E150A mutant, HEK293 cells were spinfected
629 with viral supernatants and imaged as described above where WGA (Wheat germ
630 agglutinin) conjugated with Alexa 488 was used to mark plasma membrane.
631
632 **Quantification of Orai1 and Stim1 intensities inside/outside ER-PM puncta**
633 HEK293 cells stably expressing Orai1-YFP with CFP-Stim1 or CFP-Orai1 with Stim1-YFP
634 were plated in 6 well plates and transduced with scramble or STX11 shRNA. 48hr post
635 transduction, cells were trypsinized and plated in carbon coated 35mm dishes. Images
636 were acquired using a TIRF microscope setup described before [14]. Briefly, resting cells

637 were imaged first and positions were marked. Store-depleted images were acquired after
638 incubation with 1 μM Thapsigargin (TG) and 10mM EGTA for ~6 mins. Analysis was done
639 using Otsu local thresholding in ImageJ software. Stim1 and Orai1 intensity (AU) and area
640 μm^2 values obtained from the analysis were plotted using Origin software.
641
642 **Orai:Orai FRET**
643 Scramble and STX11 shRNA transduced HEK293 cells were plated on freshly carbon
644 coated, glow discharged 35mm glass bottom dishes (IBDI) and transfected with 0.5 μg
645 each of Orai1-CFP and Orai1-YPF plasmid DNA using Lipofectamine 3000. 16 hours post
646 transfection, co-transfected cells were imaged using PlanApoN 60XO/1.42 NA
647 objective with Olympus FV3000 laser scanning microscope. Orai1-CFP, Orai1-YFP and
648 FRET images were acquired with the following excitation laser and emission bandwidth
649 parameters using DM405-445/514 dichroic mirror: CFP Ex-405nm Em-460-630nm; YFP
650 Ex-514nm Em- 530-630nm; FRET Ex-405nm, Em-530-630nm. ROIs representing the
651 plasma membrane rim were drawn around each cell, followed by local thresholding using
652 Bernsen's algorithm in Fiji software to generate an image mask which was applied to
653 CFP, YFP, FRET images to extract mean intensity values. The background subtracted
654 mean intensities of FRET (I_{FRET}), CFP (I_{Donor}) and YFP($I_{acceptor}$) images were measured
655 for each cell. Cells singly expressing Orai1-CFP or Orai1-YFP only were used as CFP
656 donor or YFP acceptor channel bleed-through (BT) controls. The BT was calculated using
657 the following formula:
658 $\mathrm{BT_{Donor}} = \frac{\mathrm{I_{FRET}}}{\mathrm{I_{Donor}}}$ when the Orai1-CFP donor alone is expressed,
659 $\mathrm{BT_{acceptor}} = \frac{\mathrm{I_{FRET}}}{\mathrm{I_{acceptor}}}$ when the Orai1-YFP acceptor alone is expressed.
660
661 FRET and NFRET percentage was calculated by subtracting the contributions of CFP
662 and YFP bleed through from the FRET signal using the following:
663 $$FRET = I_{FRET} - (BT_{Donor} * I_{Donor}) - \left(BT_{Acceptor} * I_{Acceptor}\right)$$
664

665 $$NFRET\% = \left(\frac{FRET}{\sqrt{(I_{Acceptor} * I_{Donor})}} \right) * 100$$

666

667 **Alpha-bungarotoxin binding assay**

668 U2OS cell line stably expressing Orai1-BBS-YFP construct has been described
669 previously[14]. Briefly, Orai1-BBS-YFP expressing U2OS cells were either transduced with
670 scramble shRNA/ STX11 shRNA/ pMSCV-IRES-mcherry(EV) or pMSCV-STX11-IRES-
671 mcherry. Transduced cells were trypsinized either 3-4 days post-transduction or 48 hour
672 post-transduction (in the case of pMSCV), centrifuged and labelled on ice with AF647
673 conjugated alpha-bungarotoxin (1μg/ml) containing 2% FBS in 1X HBSS for 30 mins.
674 Following this, cells were washed with HBSS and fixed with 4% PFA (~20 min at RT).
675 Samples were run using Cytoflex FACS analyzer (Beckman Coulter) and data were
676 analyzed using Flow Jo software.

677

678 **Validation of STX11 knockdown using qPCR**

679 Scramble and STX11 shRNA treated HEK293 cells were trypsinized, counted and equal
680 number of cells were used for lysis. The lysates were homogenized using QIA shredder
681 columns (Qiagen) and RNA isolation was done using RNeasy Plus Mini kit (Qiagen). Total
682 RNA isolated from both the groups was used for cDNA synthesis using oligo dT primers
683 and Superscript IV as per manufacturer's guidelines. The concentration of synthesized
684 cDNA was estimated using Qubit ssDNA assay kit and STX11 TaqMan probes were used
685 to perform the qPCR using LightCycler 96 (Roche). Beta-actin was used as housekeeping
686 control.

687

688 **Single cell Ca^{2+} imaging**

689 Cells were plated in carbon-coated glass bottom dishes (one day prior or 30 mins before
690 the assay for HEK293 and Jurkat T cells respectively) and loaded with 1μM Fura-2 AM
691 dye in HBSS ($CaCl_2$ 1.8mM, KCl 5.36mM, $MgSO_4$ 0.81mM, NaCl 136.89 mM, Na_2HPO4
692 0.335mM, D-Glucose 5.55mM) for 30 mins, at 37°C in the dark. After incubation, cells
693 were washed and incubated in Ringer's buffer (135mM NaCl, 5mM KCl, 1.8mM $CaCl_2$,

694 1mM $MgCl_2$, 5.6mM Glucose, 10mM HEPES) for an additional 10 mins, washed and
695 imaged in Ringer's buffer or Calcium-free Ringer's buffer (135mM NaCl, 5mM KCl, 1mM
696 $MgCl_2$, 5.6mM Glucose, 10mM HEPES at pH7.5), as indicated. Olympus IX-71 inverted
697 microscope equipped with a Lamda-LS illuminator (Sutter Instrument, Novato, CA), Fura-
698 2 (340/380) filter set (Chroma, Bellows Falls, VT), a 10X 0.3NA objective lens (Olympus,
699 UPLFLN, Japan), and a Photometrics Coolsnap HQ2 CCD camera was used to capture
700 images at a frequency of ~1 image pair every 2 or 4 seconds interval. Data were acquired,
701 analyzed and plotted using MetaFluor (Molecular Devices, Sunnyvale, CA), Microsoft
702 Excel, and Origin softwares. Approximately 30-40 cells were imaged per group in each
703 experiment unless otherwise stated. Mean SOCE ± SE for each experiment was
704 calculated from three independent experiments where the maximum value of the
705 scramble shRNA group (amongst the three experiments) was set at 100% and the relative
706 responses of other scr and STX11 shRNA groups were normalized w.r.t it.
707 For constitutive calcium influx assay, shRNA treated HEK293 cells were either
708 transfected or nucleofected with Orai1-S-S-EGFP, Orai1(H134S)-YFP or Orai1(ANSGA)-
709 YFP and ~12-14 hour post transfection (~4-5 hour post nucleofection), cells were loaded
710 with Fura-2 AM, washed and imaged in Ringer's buffer with 0 mM calcium to acquire
711 baselines and 2 mM calcium thereafter. To measure CAD induced constitutive calcium
712 influx, Orai1-CFP expressing stable HEK293 cells were nucleofected with YFP-CAD and
713 analyzed ~4 hour later as described above. To identify cells expressing Orai1 mutants
714 and fusion proteins in the plasma membrane, cells were imaged using a 20X 0.7NA water
715 objective lens (Olympus, UApoN340, Japan). Images were acquired at a frequency of ~1
716 image pair every 10 seconds interval to avoid photobleaching and analyzed as described
717 above.
718
719 **Measurement of NFAT nuclear localization by Western blot**
720 Jurkat T cells were transduced with scramble or STX11 shRNA to knock-down STX11 as
721 described above. On day 4 post-transduction, cells were collected, spun down and
722 resuspended in plain RPMI media and rested for 1hr at 37°C. Following this, cells were
723 counted and divided into two equal groups. One group was resuspended in RPMI
724 (unstimulated) and the other in RPMI media containing 1 μM TG + 10 ng/ml PMA (Phorbol

725 Myristate Acetate) (stimulated) and incubated at 37°C for 30 mins. Following incubation,
726 cells were pelleted and the nuclear and cytosolic protein fractions were separated using
727 NE-PER kit according to the manufacturer's guidelines and subjected to SDS-PAGE and
728 western blot using the mouse anti-NFATc2 primary antibody (Santa Cruz) followed by
729 Donkey anti-mouse secondary antibody.
730
731 **Estimation of nuclear translocation of NFAT by immunolabeling**
732 Control and STX11 depleted Jurkat T cells were rested in plain RPMI for ~1 hour prior to
733 the assay. ~100,000 cells per group were plated on freshly carbon-coated coverslips for
734 40 minutes and stimulated for 1 hour at 37°C with 5 μg/ml anti-CD3 antibody, diluted in
735 plain RPMI. Following this, cells were washed and fixed using 4% PFA diluted in 1X PBS
736 for 20 minutes at RT, washed twice and incubated with 30 mM Glycine for 10 minutes at
737 RT. For permeabilization and blocking, cells were incubated with 0.1% Saponin, 3% BSA
738 diluted in 1X PBS for 1 hour at RT, washed and incubated with anti-NFAT primary
739 antibody (anti-NFAT1, CST) at 4°C, overnight. Following primary antibody application,
740 cells were washed with 1X PBS and incubated with anti-Rabbit AF647 secondary
741 antibody for 1 hour, washed and stained with DAPI for 5 minutes followed by additional
742 washes. Images were acquired in the FV3000 confocal microscope using a 100X
743 objective lens. DAPI was used to identify the nuclear area. Nuclear *versus* whole cell
744 (total) NFAT mean intensity ratio was plotted across different groups.
745
746
747 **Whole cell lysates (WCLs), Western blot and Co-immunoprecipitation (Co-IP)**
748 HEK293 cells transfected with the desired plasmids were lysed using buffer containing
749 50 mM Tris-Cl (pH 8.0), 150 mM NaCl, 1% NP-40, 1 mM PMSF, and protease inhibitor
750 cocktail. The whole cell lysates were centrifuged at 21000 g for 15 minutes and
751 supernatants were subjected to SDS-PAGE, and western blot. For immunoprecipitations,
752 lysates were divided into two equal parts. To the first tube, the appropriate anti-mouse or
753 anti-rabbit primary antibody was added and to the second, same amount of the respective
754 IgG control antibody was added. The antibody-lysate mixtures were incubated overnight
755 at 4°C. Following this, Protein A/G Mag Sepharose beads were added and incubated with

756 the antibody-lysate mixtures for 4 hours, washed with the lysis buffer containing 0.1% NP-
757 40, boiled with 1X Laemmli buffer + 120 mM DTT and subjected to SDS-PAGE and
758 western blot analysis. Typically, 1/10th of the whole cell lysate (WCL) was loaded in the
759 input lane of the co-IP blots.
760
761 ***E. coli* expression and *in-vitro* binding assays**
762 Full-length His_6-tagged Stx11 and truncation mutants were cloned in pET28b, expressed
763 in Lemo21 (DE3) *E. coli* cells and induced with 1 mM IPTG (Isopropyl β- d-1-
764 thiogalactopyranoside) for 14-18 hours at 18°C. The cell pellets were lysed in buffer
765 containing 50 mM Tris-Cl (pH 8.0), 150 mM NaCl, 10% Glycerol, 1 mM PMSF, 1%
766 Sarkosyl, 0.1 mg/ml Lysozyme, protease inhibitor cocktail and sonicated on ice. DNase I
767 was added after sonication and the lysates were further incubated for ~60 minutes before
768 centrifugation at 21000 g for 40 mins. The supernatants were subjected to SDS-PAGE to
769 confirm expression by Coomassie staining and subsequently used for pull-down assays.
770 MBP-tagged Orai1 constructs were expressed in Lemo21 (DE3) *E. coli* cells, induced with
771 0.3mM IPTG (Isopropyl β- d-1-thiogalactopyranoside) for 14-18 hours at 18°C. The cell
772 pellets were lysed in buffer containing 50 mM Tris-Cl (pH 8.0), 150 mM NaCl, 5% Glycerol,
773 1 mM PMSF, 0.1 mg/mL Lysozyme and protease inhibitor cocktail (1:200) and sonicated
774 on ice. DNase I was added after sonication and the lysates were further incubated for ~60
775 minutes before centrifugation at 21000 g for 40 mins. The supernatants were collected
776 and subjected to SDS-PAGE to confirm expression by Coomassie staining and used for
777 pull-down assays. Following lysis, the His_6-tagged Stx11 proteins were purified using
778 Talon Beads and MBP-tagged Orai1 proteins using Dextrin Sepharose/Amylose resin
779 according to the manufacturer's guidelines. For *in-vitro* binding assays, lysates prepared
780 from cells expressing MBP or MBP-tagged Orai1 fragments were incubated with 25 μL
781 Dextrin Sepharose Beads and incubated for 2 hours at 4°C. After incubation, beads were
782 washed thrice and ~50-125 ng of purified His-tagged full length Stx11, His-tagged SNARE
783 or His-tagged H_{abc} domains were diluted in buffer containing 50mM Tris-Cl (pH8), 150
784 mM NaCl, 5% Glycerol and 0.1% NP-40 and added to the beads. Following 1 hour of
785 incubation at 4°C, the beads were washed thrice, re-suspended and boiled in the binding
786 buffer containing 1X Laemmli and 120 mM DTT. The eluate was subjected to SDS-PAGE

787 and Western blot. MBP and MBP-tagged proteins were detected with Ponceau staining,
788 Full length STX11 using Rabbit anti-STX11 primary antibody (Thermo) followed by
789 Donkey anti-rabbit HRP and His-tagged STX11 fragments were detected or mouse anti-
790 6XHis primary antibody (Invitrogen) followed by Donkey anti-mouse HRP secondary
791 antibody.
792
793 **qPCR to estimate gene expression in Jurkat T cells**
794 Scramble (scr) and STX11 shRNA treated Jurkat T cells were rested for ~1 hour prior to
795 the assay, stimulated with soluble anti-CD3 (5-10 μg/ml) for 3 hours and washed with
796 HBSS. Total RNA was isolated using RNeasy Mini kit as per manufacturer's instructions.
797 cDNA was synthesized using random hexamers and Invitrogen Superscript IV kit and
798 quantified using Qubit ssDNA assay. Taqman probes for IL-2 and beta-actin
799 housekeeping control were used for performing the qPCR in triplicates. Data analysis was
800 done by calculating the double delta C_t values.
801
802 **EIA to measure IL-2 level in cell supernatant of Jurkat T cells**
803 Scramble (scr) and STX11 shRNA treated Jurkat T cells were stimulated with plate-
804 coated anti-CD3 (10 μg/ml) and the culture supernatants were collected at 12 and 24 hour
805 post-stimulation. EIA plates were coated with purified mouse anti-human IL-2 capture
806 antibody (1 μg/ml) overnight at 4°C, washed with 0.05% PBST and blocked with 2% BSA
807 for 2 hours. After blocking, the plates were incubated with the culture supernatants for 2
808 hours at RT, washed and incubated with the detection antibody (Biotin mouse anti-human
809 IL-2, 1 μg/ml) for 2 hours. After washing, Streptavidin HRP (0.1 μg/ml) followed by TMB
810 reagent were added. 250 mM HCl was added to stop the reaction and absorbance was
811 measured at 450 nm.
812
813 **Isolation and culture of human PBMCs**
814 Whole blood freshly collected in Heparin or Citrate Phosphate Dextrose Adenine (CPDA)
815 solution was subjected to density gradient centrifugation using Ficoll-Paque PLUS media.
816 The buffy coat was separated, washed twice with HBSS and cultured with IL-2 (50 ng/ml).
817 Cells were stimulated once per week with PHA (2 μg/ml) for 72 hours and rested in IL-2

818 for the remaining 72-96 hours. Unless specified, all the assays were performed following
819 24-48 hours of rest, post stimulation.
820
821 **Isolation of genomic DNA and sequencing**
822 Genomic DNA was extracted from PBMCs using Phenol-Chloroform-Isoamyl alcohol.
823 STX11 genomic region flanking the mutation was PCR amplified using primers: 5'
824 Forward -CATGCACGACTACAACCAGGC and 3' Reverse -
825 GGGACAGCAGAAGCAGCAGAGGG. The resulting PCR products were separated on
826 2% agarose gel, excised and extracted using the Macherey-Nagel Nucleospin columns
827 and subjected to Sanger sequencing using the 5' Forward PCR primer to confirm the
828 mutation.
829
830 **Measurement of SOCE in human PBMCs**
831 PBMCs in culture were washed, rested and allowed to adhere to freshly carbon-coated
832 (IBDI) dishes for 1 hour in plain RPMI at 37°C. The cells were washed with HBSS and
833 incubated with 1 ml of 1 μM Fura-2-AM diluted in Ringer's buffer for 40 minutes, washed
834 and incubated for an additional 10 minutes to allow de-esterification of the dye. The assay
835 was started with 1 ml of Calcium free Ringer's buffer in the imaging dish and images were
836 captured every 4 seconds. After capturing the baseline for ~60 seconds, stores were
837 depleted by the addition of 1 μM Thapsigargin. In other assays, 10 μg/ml of anti-CD3 and
838 5 μg/ml of the secondary antibody were used to cross-link the TCRs and thereby induce
839 store depletion. ~5 minutes post-store-depletion, Calcium Chloride ($CaCl_2$) was added
840 back to the dish at a final concentration of 2 mM to estimate the magnitude of store
841 operated calcium entry.
842
843 **Degranulation assay**
844 PBMCs were cultured in RPMI containing 10% FBS and 50 ng/ml IL-2 and stimulated
845 with PHA (2 μg /ml) 48hrs before the assay. 24hrs prior to the assay, IL-2 was washed
846 off but PHA was re-added. On the day of the assay cells were washed twice to remove
847 PHA and any growth factors. To measure degranulation, cells were either left
848 unstimulated, stimulated with a combination of anti-CD3 (10 μg/ml plate-coated), anti-

849 CD28 (2 μg/ml soluble) and anti-CD49d (2 μg/ml soluble) or a combination of Ionomycin
850 (1 μM) and PMA (50 ng/ml) for 3.5 hours. CD107a-PE antibody (1:50 dilution) was added
851 to each of the three groups at the start of stimulation. Following stimulations, cells were
852 transferred to ice, washed with cold HBSS containing 2% FBS and incubated with anti-
853 CD8 APC for 20 minutes, washed twice with cold HBSS and analyzed using Cytoflex
854 (Beckman Coulter) flow cytometer.
855
856 **qPCR to estimate gene expression in human PBMCs**
857 PBMCs were taken off IL-2 48 hours prior to the assay. On the day of the assay, cells
858 were washed twice, left unstimulated and either stimulated with anti-CD3 (10 μg/ml, plate-
859 coated), anti-CD28 (2 μg/ml) and anti-CD49d (2 μg/ml) or with Ionomycin (1 μM) and PMA
860 (50 ng/ml) for 6 hours. To end the stimulation, cells were washed with cold HBSS, pelleted
861 and used for RNA extraction. Total RNA was isolated using Qiagen RNeasy mini kit and
862 cDNA was synthesized using random hexamers and Superscript IV (Invitrogen). cDNA
863 was quantified using Qubit and subjected to QPCR analysis using Taqman probes for IL-
864 2 and beta-actin housekeeping gene control in triplicates. Analysis was performed by
865 calculating the double delta C_t values.
866
867 **Transduction of human PBMCs with pMSCV-STX11**
868 For viral transduction of PBMCs, polystyrene non-TC treated 24-well plates were coated
869 with retronection (20 μg/ml) overnight at 4°C, blocked with 2% BSA for 30 minutes at
870 room temperature and washed twice with HBSS. The retroviral supernatants were added
871 onto the coated wells and the plates were spun at 1800g for 2 hours at 30°C. Following
872 spin, the wells were washed with the blocking solution. PBMCs cultured in RPMI
873 containing 10% FBS were stimulated with PHA (2 μg/ml) and IL-2 (50 ng/ml) for 48 hours
874 prior to transduction. Stimulated PBMCs were transferred to coated plates at a density of
875 0.25 million cells/well centrifuged at 400g for 40 minutes at 30°C. The cells were analyzed
876 48-72 hours post transduction.
877
878 **Patch clamp measurements**

879 Patch clamp recordings were performed by using an Axopatch 200B amplifier (Axon
880 Instruments, Foster City, CA) interfaced to an ITC-18 input/output board (Instrutech, Port
881 Washington, NY) and an iMac G5 computer. Currents were filtered at 1 kHz with a four-
882 pole Bessel filter and sampled at 5 kHz. Recording electrodes were pulled from 100-µl
883 pipettes (VWR), coated with Sylgard, and fire-polished to a final resistance of 2 to 5 MΩ.
884 Stimulation and data acquisition and analysis were performed by using in-house routines
885 developed by RS Lewis (Stanford University) on the Igor Pro platform (Wavemetrics, Lake
886 Oswego, OR). All data were corrected for the liquid junction potential of the pipette
887 solution relative to Ringer's in the bath (-10 mV) and for leak currents collected in 20 mM
888 extracellular free calcium plus 10µM La^{3+}. The holding potential was +30 mV. The
889 standard voltage stimulus consisted of a 100-ms step to –100 mV followed by a 100-ms
890 ramp from –100 to +100 mV applied at 1 s intervals. I_{CRAC} was typically activated by
891 passive depletion of ER Ca^{2+} stores by intracellular dialysis of 8 mM BAPTA.
892
893 **Solutions and chemicals**
894 The standard extracellular Ringer solution contained 130 mM NaCl, 4.5 mM KCl, 20 mM
895 $CaCl_2$, 10 mM tetraethylammoniumchloride (TEA-Cl), 10 mM D -glucose and 5 mM
896 HEPES (pH 7.4 with NaOH). The standard divalent-free (DVF) Ringer solutions contained
897 (in mM) 150 NaCl, 10 HEDTA, 1 EDTA, and 10 HEPES (pH 7.4). The internal solution
898 contained: 135 mM Cs aspartate, 8 mM $MgCl_2$, 8 mM Cs-BAPTA and 10 mM HEPES (pH
899 7.2 with CsOH).
900
901 **Data analysis**
902 Analysis of current amplitudes was typically performed by measuring the peak currents
903 during the -100 mV pulse. Averaged results are presented as the mean value standard
904 error of the mean (SEM). Reversal potentials were measured from the average of several
905 leak-subtracted sweeps (4–6) in each cell. For datasets with two groups, statistical
906 analysis was performed with two- tailed t test to compare between control and test
907 conditions with a confidence level of 95%, and results with $p<0.05$ were considered
908 statistically significant.
909

910 **STX11:Orai1 and Stim1:Orai complex prediction**

911 Full length STX11 and its two domains, (H_{abc} 41-167 and SNARE 183-267) and Orai1 (N-
912 terminus 1-87 and C-terminus 256-301) were used to generate the complex of STX11
913 and Orai1 using AlphaFold3 (AF3) in all combinations. For Stim1, residue 312- 387 were
914 used along with Orai C-terminus 256-301. The resultant models were assessed using
915 ipTM and pTM scores. The best scoring combinations were further considered to
916 generate more models by changing the seed values. The best model in terms of highest
917 ipTM and pTM values was considered for further analysis. Custom script was used to
918 analyze the contact frequency of interacting residues of STX11-H_{abc} and Orai1 C-terminus
919 complex as well as Stim1 and Orai1 C-terminus, across all predicted models.

920

921 **Molecular dynamics (MD) simulation**

922 The STX11 H_{abc}:Orai1 C-terminus and Stim1(312-387):Orai1 C-terminus complexes were
923 subjected to all-atom MD simulations. Initially, the complexes was prepared using protein-
924 preparation module of Schrodinger which involves H-bond network optimization and
925 restrained minimization of the initial structure. The prepared structures were solvated
926 using TIP3P water model in an orthorhombic box and neutralized by adding counter ions.
927 OPLS4 force field was used, and simulation system was generated by specifying 150 mM
928 salt (NaCl). The solvated system was subjected to default relaxation protocol of Desmond
929 followed by production run for 500 ns at 300K and 1 atm pressure in NPT ensemble. The
930 default relaxation protocol includes several short simulation steps. (1) Brownian dynamics
931 simulation for 100 ps at 10 K temperature in NVT with restraints on solute heavy atoms
932 (2) Simulation in NVT ensemble at 10 K for 12 ps with restraints on solute heavy atoms
933 (3) 12 ps simulation in NPT ensemble at 10 K with restraints on solute heavy atoms (4)
934 Simulation in NPT ensemble for 12 ps with restraints on solute heavy atoms (5) Simulation
935 in NPT ensemble for 24 ps without restraints. Three independent runs were executed with
936 different initial seeds for both structures.

937

938 **Analysis of MD simulation**

939 The MD runs were analyzed for the stability of the complex and interactions between the
940 subunits. The RMSD was calculated using simulation interaction diagram (SID) module

941 of Schrodinger. The first frame was used as reference frame for RMSD calculation. Script
942 “analyze_trajectory_ppi.py” was used to calculate the interactions between STX11:Orai1
943 and Stim1:Orai1. The binding energy (ΔG) at each nanosecond across simulation was
944 calculated using “thermal_mmgbsa.py” script of Schrodinger. The representative
945 structure was generated through trajectory clustering. The last 200 ns frames from each
946 run were combined and clustered using scripts “trj_merge.py” and “trajectory cluster” of
947 Schrodinger. The cluster representative of the largest cluster was used to analyze the
948 protein-protein interactions. PDB Sum was used to calculate the interactions in the cluster
949 representative. Figures were generated using Pymol and MD movies using Maestro.
950
951 **Statistical Analysis**
952 Statistical analysis was done using unpaired two-tailed Student’s *t* test where only two
953 groups were being compared and ANOVA where more than two groups were present.
954 Normality of distribution was checked in Origin. Mann Whitney U Test was used for
955 datasets with non-normal (or skewed) distribution. P values for all significance tests were
956 *P<0.05; **P<0.01; ***P<0.001.
957
958
959 **Acknowledgements:** We thank Vivien Beziat, Yenan Bryceson, Heinrich Schlums, Jelve
960 Nejati Zendegani, Stephan Ehl, and Jasmin Mann for help with human PBMC handling,
961 isolation, storage and shipping. Anand Vaidya for advice on STX11 purification. Jyoti
962 Rohilla for technical support. Bio Render for the generation of models and IBS 2.0 for the
963 generation of schematics shown in this manuscript. This work was supported in part by
964 Department of Atomic Energy, Government of India under Project Identification
965 No. RTI 4007 and NIH-NIAID grant AI108636.
966
967
968
969
970
971

References:

1. Zhang, K., et al., *Familial Hemophagocytic Lymphohistiocytosis*, in *GeneReviews((R))*, M.P. Adam, et al., Editors. 1993: Seattle (WA).
2. D'Orlando, O., et al., *Syntaxin 11 is required for NK and CD8(+) T-cell cytotoxicity and neutrophil degranulation.* Eur J Immunol, 2013. **43**(1): p. 194-208.
3. Clapham, D.E., *Calcium signaling.* Cell, 2007. **131**(6): p. 1047-58.
4. Vig, M. and J.P. Kinet, *The long and arduous road to CRAC.* Cell Calcium, 2007. **42**(2): p. 157-62.
5. Vig, M., et al., *Defective mast cell effector functions in mice lacking the CRACM1 pore subunit of store-operated calcium release-activated calcium channels.* Nat Immunol, 2008. **9**(1): p. 89-96.
6. Maul-Pavicic, A., et al., *ORAI1-mediated calcium influx is required for human cytotoxic lymphocyte degranulation and target cell lysis.* Proc Natl Acad Sci U S A, 2011. **108**(8): p. 3324-9.
7. Vig, M., et al., *CRACM1 multimers form the ion-selective pore of the CRAC channel.* Curr Biol, 2006. **16**(20): p. 2073-9.
8. Vig, M., et al., *CRACM1 is a plasma membrane protein essential for store-operated Ca2+ entry.* Science, 2006. **312**(5777): p. 1220-3.
9. Miao, Y., et al., *An essential and NSF independent role for alpha-SNAP in store-operated calcium entry.* Elife, 2013. **2**: p. e00802.
10. Prakriya, M. and R.S. Lewis, *Store-Operated Calcium Channels.* Physiol Rev, 2015. **95**(4): p. 1383-436.
11. Feske, S., et al., *A mutation in Orai1 causes immune deficiency by abrogating CRAC channel function.* Nature, 2006. **441**(7090): p. 179-85.
12. Zhang, S.L., et al., *Genome-wide RNAi screen of Ca(2+) influx identifies genes that regulate Ca(2+) release-activated Ca(2+) channel activity.* Proc Natl Acad Sci U S A, 2006. **103**(24): p. 9357-62.
13. Yoon, T.Y. and M. Munson, *SNARE complex assembly and disassembly.* Curr Biol, 2018. **28**(8): p. R397-R401.
14. Li, P., et al., *alpha-SNAP regulates dynamic, on-site assembly and calcium selectivity of Orai1 channels.* Mol Biol Cell, 2016. **27**(16): p. 2542-53.
15. Miao, Y., et al., *Na+ influx via Orai1 inhibits intracellular ATP induced mTORC2 signaling to disrupt CD4 T cell gene expression and differentiation.* Elife, 2017. **6**.
16. Ramanagoudr-Bhojappa, R., Y. Miao, and M. Vig, *High affinity associations with alpha-SNAP enable calcium entry via Orai1 channels.* PLoS One, 2021. **16**(10): p. e0258670.
17. Jarvis, S.E. and G.W. Zamponi, *Masters or slaves? Vesicle release machinery and the regulation of presynaptic calcium channels.* Cell Calcium, 2005. **37**(5): p. 483-8.
18. Lu, Q., et al., *Syntaxin 1A supports voltage-dependent inhibition of alpha1B Ca2+ channels by Gbetagamma in chick sensory neurons.* J Neurosci, 2001. **21**(9): p. 2949-57.
19. Bezprozvanny, I., R.H. Scheller, and R.W. Tsien, *Functional impact of syntaxin on gating of N-type and Q-type calcium channels.* Nature, 1995. **378**(6557): p. 623-6.

1014 20. Vig, M. and J.P. Kinet, *Calcium signaling in immune cells.* Nature immunology, 2009.
1015 **10**(1): p. 21-7.
1016 21. Bryceson, Y.T., et al., *Defective cytotoxic lymphocyte degranulation in syntaxin-11*
1017 *deficient familial hemophagocytic lymphohistiocytosis 4 (FHL4) patients.* Blood, 2007.
1018 **110**(6): p. 1906-15.
1019 22. Hackmann, Y., et al., *Syntaxin binding mechanism and disease-causing mutations in*
1020 *Munc18-2.* Proc Natl Acad Sci U S A, 2013. **110**(47): p. E4482-91.
1021 23. Hellewell, A.L., et al., *Analysis of familial hemophagocytic lymphohistiocytosis type 4*
1022 *(FHL-4) mutant proteins reveals that S-acylation is required for the function of syntaxin*
1023 *11 in natural killer cells.* PLoS One, 2014. **9**(6): p. e98900.
1024 24. Jahn, R. and R.H. Scheller, *SNAREs--engines for membrane fusion.* Nat Rev Mol Cell Biol,
1025 2006. **7**(9): p. 631-43.
1026 25. Stathopulos, P.B., et al., *STIM1/Orai1 coiled-coil interplay in the regulation of store-*
1027 *operated calcium entry.* Nat Commun, 2013. **4**: p. 2963.
1028 26. Peinelt, C., et al., *Amplification of CRAC current by STIM1 and CRACM1 (Orai1).* Nat Cell
1029 Biol, 2006. **8**(7): p. 771-3.
1030 27. Mercer, J.C., et al., *Large store-operated calcium selective currents due to co-expression*
1031 *of Orai1 or Orai2 with the intracellular calcium sensor, Stim1.* J Biol Chem, 2006.
1032 **281**(34): p. 24979-90.
1033 28. Soboloff, J., et al., *Orai1 and STIM reconstitute store-operated calcium channel function.*
1034 J Biol Chem, 2006. **281**(30): p. 20661-20665.
1035 29. Penna, A., et al., *The CRAC channel consists of a tetramer formed by Stim-induced*
1036 *dimerization of Orai dimers.* Nature, 2008. **456**(7218): p. 116-20.
1037 30. Li, Z., et al., *Graded activation of CRAC channel by binding of different numbers of STIM1*
1038 *to Orai1 subunits.* Cell Res, 2011. **21**(2): p. 305-15.
1039 31. Hou, X., S.R. Burstein, and S.B. Long, *Structures reveal opening of the store-operated*
1040 *calcium channel Orai.* Elife, 2018. **7**.
1041 32. Zhou, Y., et al., *The STIM1-binding site nexus remotely controls Orai1 channel gating.*
1042 Nat Commun, 2016. **7**: p. 13725.
1043 33. Cormet-Boyaka, E., et al., *CFTR chloride channels are regulated by a SNAP-23/syntaxin*
1044 *1A complex.* Proc Natl Acad Sci U S A, 2002. **99**(19): p. 12477-82.
1045 34. Toft-Bertelsen, T.L., et al., *Regulation of Ca2+ channels by SNAP-25 via recruitment of*
1046 *syntaxin-1 from plasma membrane clusters.* Mol Biol Cell, 2016. **27**(21): p. 3329-3341.
1047 35. Jessen, B., et al., *Graded defects in cytotoxicity determine severity of hemophagocytic*
1048 *lymphohistiocytosis in humans and mice.* Front Immunol, 2013. **4**: p. 448.
1049 36. Chinn, I.K., et al., *Genetic and mechanistic diversity in pediatric hemophagocytic*
1050 *lymphohistiocytosis.* Blood, 2018. **132**(1): p. 89-100.
1051 37. Park, C.Y., et al., *STIM1 clusters and activates CRAC channels via direct binding of a*
1052 *cytosolic domain to Orai1.* Cell, 2009. **136**(5): p. 876-90.
1053 38. Delevoye, C., et al., *Conservation of the biochemical properties of IncA from Chlamydia*
1054 *trachomatis and Chlamydia caviae: oligomerization of IncA mediates interaction*
1055 *between facing membranes.* J Biol Chem, 2004. **279**(45): p. 46896-906.
1056 39. Paumet, F., et al., *Intracellular bacteria encode inhibitory SNARE-like proteins.* PLoS One,
1057 2009. **4**(10): p. e7375.

40. Barocchi, M.A., V. Masignani, and R. Rappuoli, *Opinion: Cell entry machines: a common theme in nature?* Nat Rev Microbiol, 2005. **3**(4): p. 349-58.
41. Neveu, E., et al., *Prototypic SNARE Proteins Are Encoded in the Genomes of Heimdallarchaeota, Potentially Bridging the Gap between the Prokaryotes and Eukaryotes.* Curr Biol, 2020. **30**(13): p. 2468-2480 e5.

1091

1092 **Figure Legends:**

1093

1094 **Figure 1: STX11 is required for SOCE.** Measurement of SOCE in STX11 depleted
1095 Jurkat and FHLH4 patient T cells. (**A-B**) Representative Fura-2 calcium imaging assay
1096 (**A**) and quantification of independent repeats (**B**) measuring thapsigargin (TG) induced
1097 SOCE in Jurkat T cells treated with scr (black), STX11#1 (red) or STX11#2 (blue)
1098 shRNAs. (n=30-40 cells/group, N=3). (**C-D**) Representative Fura-2 calcium imaging
1099 assay (**C**) and quantification of repeats (**D**) showing reconstitution of SOCE in STX11
1100 depleted Jurkat T cells by ectopic expression of STX11. scr shRNA with empty vector
1101 (EV) expression (black), STX11 shRNA with EV expression (red), STX11 shRNA with
1102 STX11 expression (green). (**E**) Sanger sequencing of FHLH4 patient DNA showing
1103 deletion of a single Adenine at the 752nd position and the resulting frameshift. (**F**)
1104 Schematic showing the predicted domain distribution of the wildtype *versus* FHLH4
1105 mutant STX11 protein. (**G**) Western blot on WCLs of healthy donor (HD) and FHLH4
1106 patient PBMCs showing the relative molecular weight and abundance of the wildtype and
1107 mutant STX11 bands. (**H**) Western blot on WCLs of HEK293 cells over-expressing
1108 wildtype or FHLH4 mutant STX11 and empty vector. (**I**) Fura-2 calcium imaging assay
1109 measuring anti-CD3 induced SOCE in HD (black) and FHLH4 (red) T cells. (n=30-40
1110 cells/group). (**J**) Fura-2 calcium imaging assay measuring SOCE in HD expressing empty
1111 vector (EV) (black) and FHLH4 T cells expressing human STX11 (red), respectively.
1112 (n=30-40 cells/group). (**K-L**) Representative Fura-2 calcium imaging assay (**K**) and
1113 quantification of repeats (**L**) measuring SOCE in Jurkat T cells treated either with scr
1114 shRNA expressing empty vector (EV) (black), STX11 shRNA, expressing EV (red),
1115 STX11 shRNA, expressing wildtype STX11 (green), STX11 shRNA, expressing FHLH4
1116 mutant STX11 (blue).

1117 **Figure 2. STX11 regulates I_{CRAC}.** Effect of over-expression of STX11 on SOCE and
1118 measurement of I_{CRAC}. (**A-B**) Representative Fura-2 calcium imaging assay (**A**) and
1119 quantification of repeats (**B**) measuring SOCE in HD PBMCs, expressing empty vector
1120 (EV) (black) or wildtype STX11 (red). (**C-D**) Dependence of STX11 mediated

1121 enhancement of SOCE on Orai1. A representative Fura-2 calcium imaging assay (**C**) and
1122 quantification of repeats (**D**) showing measurement of TG induced SOCE in HEK293 cells
1123 where Orai1 was depleted and STX11 was over-expressed. Scr shRNA + empty vector
1124 (black), Orai1 shRNA + empty vector (red), Orai1 shRNA + STX11 (blue). N=3. (**E-H**)
1125 Measurement of I_{CRAC} in STX11 depleted Jurkat T-cells in the whole-cell recording
1126 configuration in 20 mM extracellular Ca^{2+} Ringer's solution. I_{CRAC} was induced by passive
1127 depletion of intracellular Ca^{2+} stores by dialyzing 8 mM BAPTA into the cell via the patch-
1128 pipette. (**E**) Representative current at -100 mV in Jurkat T cells treated with scr shRNA
1129 construct. The current is blocked by extracellular La^{3+} (10 μM) and replacing the 20 mM
1130 Ca^{2+} Ringer's solution with a divalent free solution (DVF) evokes a large Na^{+} current which
1131 depotentiates over tens of seconds. The current-voltage (I-V) relationship of the Ca^{2+} and
1132 DVF currents are shown on the right. (**F**) I_{CRAC} from a Jurkat T cell treated with STX11
1133 shRNA. Both Ca^{2+} and Na^{+} current amplitudes are reduced relative to control cells. The
1134 I-V relationships (*right plots)* show no change in ion selectivity. (**G-H**) Summary of the
1135 current amplitudes of Ca^{2+} and Na^{+} currents and current reversal potentials in scr and
1136 STX11 knockdown cells.

1137 **Figure 3. STX11 regulates NFAT activation, IL-2 gene expression and degranulation**
1138 **in FHLH4 patient T cells.** (**A-C**) Estimation of nuclear translocation of NFAT. (**A**) Western
1139 blot showing nuclear translocation of NFAT in Jurkat T cells treated with scr or STX11
1140 shRNA and stimulated with PMA+TG. N=3. (**B**) Representative confocal images of control
1141 and STX11 depleted Jurkat T cells stimulated with anti-CD3, immunolabelled with anti-
1142 NFAT1 antibody and counter-stained with DAPI. (N=3) (**C**) Box and whisker plot showing
1143 quantification of nuclear NFAT from cells populating 10 randomly chosen fields per group
1144 in (**B**). (**D**) Quantification of IL-2 mRNA in anti-CD3 stimulated Jurkat T cells treated with
1145 scr or STX11 shRNA using qPCR. The bars show mean ± SE of relative IL-2 mRNA. N=3.
1146 (E) Quantification of IL-2 EIA on supernatants of scr (black) or STX11 (red) shRNA treated
1147 Jurkat T cells stimulated with anti-CD3. (**F**) qPCR analysis of IL-2 mRNA expression in
1148 various stimulated HD (black) and FHLH4 T cells (red). (**G-H**) Granule release assay
1149 performed on HD (black) and FHLH4 CD8 T (red) cells (**G**) and its quantification (**H**).
1150

1151 **Figure 4: STX11 directly binds resting Orai1 in plasma membrane.** Intracellular
1152 localization of STX11 and its association with Orai1. (**A**) Representative confocal images
1153 of HEK293 cells expressing Orai1-YFP with either STX11 or empty vector (Vector),
1154 stained using anti-STX11 antibody. N=3. (**B-C**) Co-IP to assess STX11 binding to Orai1.
1155 Whole cell lysates of resting and store-depleted HEK293 cells co-expressing either Flag-
1156 Orai1 and STX11 (**B**) or Orai1-Myc and STX11 (**C**) were subjected to IP and western blot
1157 using anti-Myc, anti-Flag or anti-STX11 antibodies, as indicated. (N=3) **(D)** Schematic
1158 showing key domains of STX11 and Orai1 used for *in vitro* pull-down assays. (**E**) Pull-
1159 down assay showing *in vitro* binding of His-tagged STX11 to Orai1. (Top) Ponceau S
1160 staining showing the input of MBP alone or MBP-tagged Orai1 fragments. (Bottom)
1161 Western blot using anti-STX11 antibody. Input:1/5th of the protein. N=4. (**F**) Pull-down
1162 assay showing *in vitro* binding of His-tagged H_{abc} domain of STX11 to Orai1 fragments.
1163 (Top) Ponceau S staining showing the input of MBP alone or MBP-tagged Orai1
1164 fragments. Input:1/5th of the protein. (Bottom) Western blot using anti-His antibody. N=3.
1165 (**G**) Binding free energy distribution of STX11-H_{abc} and Orai1 C-terminus interactions. (**H**)
1166 Sphere and cartoon representation of the structure of STX11 H_{abc} (green) and Orai1 C-
1167 terminus (cyan) complex after MD simulation. The N-termini are highlighted in blue, and
1168 C-termini in red. (**I**) Representative confocal images showing localization of STX11 with
1169 respect to Orai1:Stim1 puncta in store-depleted cells. HEK293 cells expressing Orai1-
1170 YFP, CFP-Stim1 were transfected with STX11 and stained using anti-STX11 antibody.
1171 (N=3) (**J-K**) Binding free energy distribution for the interactions between the protomers
1172 (**J**) and dimers (**K**) of Stim1(312-387) and Orai1 C-terminus interactions. (N=3)
1173
1174 **Figure 5. Residues involved in Orai1:STX11 complex formation are crucial for**
1175 **SOCE.** Analysis of STX11 and Orai1 mutants. (**A**) Schematic showing STX11 mutations
1176 (Top). Expression of wildtype STX11 or STX11 N147A_E150A mutant in HEK293
1177 followed by immunolabeling (**A**, bottom) and Western blot (**B**) using anti-STX11 antibody.
1178 (**C-D**) Representative Fura-2 calcium imaging assay (**C**) and quantification of repeats (**D**)
1179 measuring rescue of SOCE in Jurkat cells treated either with scr shRNA (black) or STX11
1180 shRNA expressing empty vector (red), wildtype STX11 (green) or N147A_E150A mutant
1181 STX11 (blue). (**E**) Coomassie blue stained SDS-PAGE showing expression and

1182 purification of His-tagged wildtype or N147A_E150A mutant STX11 from *E. coli.* (**F**) Pull-
1183 down assay measuring their binding to MBP-tagged Orai1 C-terminus. (Top) Ponceau S
1184 staining showing the input of MBP-tagged fragments. (Bottom) Western blot using anti-
1185 STX11 antibody. N=4 (**G**) Schematic showing Orai1 mutations (Top). Confocal images of
1186 HEK293 cells expressing YFP-tagged wildtype or R289A_E272A_E275A_E278A mutant
1187 Orai1 (Bottom). **(H-I)** Representative Fura-2 calcium imaging assay (**H**) and quantification
1188 of repeats (**I**) measuring rescue of SOCE in HEK293 cells treated either with scr (black)
1189 or Orai1 shRNA expressing empty vector (red), wildtype Orai1 (green) or
1190 R289A_E272A_E275A_E278A mutant Orai1 (blue). (**J**) Pull-down assay measuring the
1191 binding of MBP-tagged wildtype or R289A_E272A_E275A_E278A mutant Orai1 C-
1192 terminus to wildtype or N147A_E150A mutant STX11. (Top) Ponceau S staining showing
1193 the input of MBP-tagged Orai1 fragments. (Bottom) Western blot using anti-STX11
1194 antibody. N=4. (**K-L**) Representative confocal images (**K**) and quantification (**L**) of PM
1195 localized YFP-CAD in CFP-tagged wildtype or R289A_E272A_E275A_E278A mutant
1196 Orai1 expressing HEK293 cells.
1197
1198 **Figure 6: Functional clustering of Orai1 is compromised in STX11 depleted cells.**
1199 Quantification of Orai1 and Stim1 intensities in the ER-PM puncta of store-depleted cells.
1200 (**A-B**) Representative confocal images of resting (**A**) and store-depleted (**B**) shRNA
1201 treated HEK293 cells expressing N-terminal CFP tagged Orai1 (CFP-Orai1) and C-
1202 terminal YFP tagged Stim1 (Stim1-YFP). (**C-F**) Mean Stim1-YFP intensity (**C**) and area
1203 (**D**) of Stim1 clusters. Mean CFP-Orai1 intensities inside (**E**) and outside (**F**) Stim1-YFP
1204 clusters of shRNA treated cells, post store-depletion. (**G-J**) Quantification of Orai1 and
1205 Stim1 intensities in the ER-PM puncta of C-terminal YFP-tagged Orai1 (Orai1-YFP) and
1206 N-terminal CFP-tagged Stim1 (CFP-Stim1). (**G-H**) Mean CFP-Stim1 intensity (**G**) and
1207 area (**H**) of Stim1 clusters. Mean Orai1-YFP intensity (**I**) and area (**J**) of Orai1-YFP
1208 clusters in control and STX11 depleted cells. (**K-L**) Representative Fura-2 calcium
1209 imaging assay (**K**) and quantification of repeats (**L**) measuring TG induced SOCE in
1210 Orai1-YFP and CFP-Stim1 expressing HEK293 cells treated with scr (black) or STX11
1211 (red) shRNA.
1212

1213 **Figure 7: STX11 primes Orai1 for successful gating by Stim1.** Orai:Orai FRET. **(A)**
1214 FRET analysis of control and STX11 shRNA treated HEK293 cells co-expressing Orai1-
1215 CFP and Orai1-YFP under resting conditions. (**B**) FRET analysis of cells described in (**A**)
1216 before and after store-depletion. (**C-E**) Fura-2 calcium imaging assay (**C**) and
1217 quantification of repeats (**D-E**) to measure constitutive calcium influx in Orai1-CFP and
1218 YFP-CAD expressing, control (black) or STX11 depleted (red) HEK293 cells at 0 mM (**D**)
1219 and 2 mM (**E**) extracellular Ca^{2+}. (**F-G**) Fura-2 calcium imaging assay (**F**) and
1220 quantification of repeats (**G**) to measure constitutive calcium influx in Orai1-H134S mutant
1221 expressing control (black) and STX11 depleted (red) HEK293 cells. (**H-I**) Fura-2 calcium
1222 imaging assay (**H**) and quantification of repeats (**I**) to measure constitutive calcium influx
1223 in Orai1-ANSGA mutant expressing control (black) and STX11 depleted (red) HEK293
1224 cells. (**J**) Proposed model depicting STX11 unbound (unprimed) and bound Orai1
1225 undergoing priming and correct assembly before Stim1 mediated gating. For simplicity,
1226 interactions for only two subunits in the front have been highlighted in primed Orai1.
1227

1228 **Supplementary Movies 1-3: Molecular dynamic simulations of Orai1 C-terminus**
1229 **interaction with the STX11_H_{ABC} domain.**

1230 **Supplementary Movies 4-6: Molecular dynamic simulations of Orai1 C-terminus**
1231 **interaction with Stim1 (312-387).**
1232 Due to BioRxiv file size limit, the movies can be found at the following link:
1233 https://www.dropbox.com/scl/fo/3j07d3sua4g58w3yfmyv7/AAKjvIiniA-
1234 z994hxV9DNHo?rlkey=e7yj5wyukvwg5seg1awkuctc4&st=z6vp57dr&dl=0
1235

Figure 1

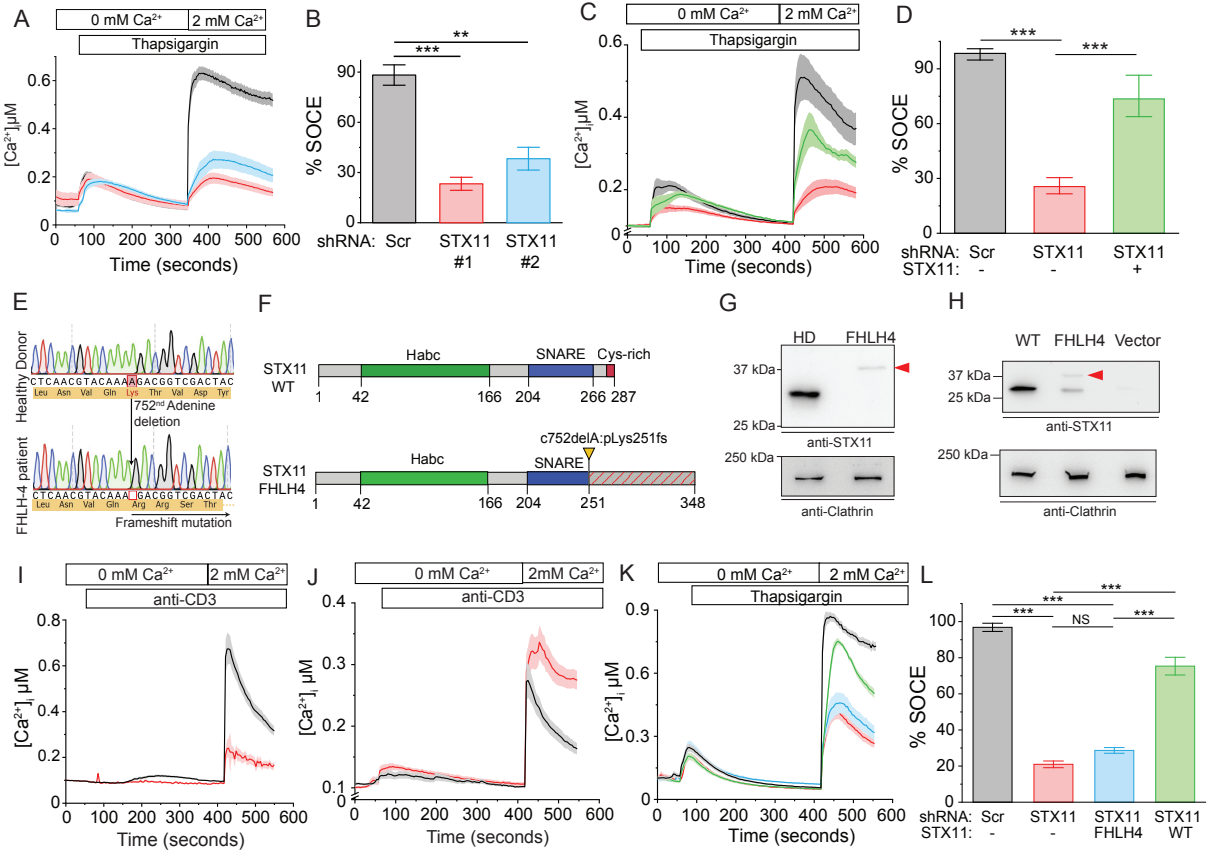
A
0 mM Ca2+
2 mM Ca2+
Thapsigargin
[Ca2+]µM
Time (seconds)
B
% SOCE
shRNA: Scr
STX11 #1
STX11 #2
C
0 mM Ca2+
2 mM Ca2+
Thapsigargin
[Ca2+]µM
Time (seconds)
D
% SOCE
shRNA: Scr
STX11: -
STX11 -
STX11 +
E
Healthy Donor
FHLH-4 patient
752nd Adenine deletion
Frameshift mutation
F
STX11 WT
Habc
SNARE
Cys-rich
STX11 FHLH4
c752delA:pLys251fs
G
HD
FHLH4
37 kDa
25 kDa
anti-STX11
250 kDa
anti-Clathrin
H
WT
FHLH4
Vector
37 kDa
25 kDa
anti-STX11
250 kDa
anti-Clathrin
I
0 mM Ca2+
2 mM Ca2+
anti-CD3
[Ca2+]i µM
Time (seconds)
J
0 mM Ca2+
2mM Ca2+
anti-CD3
[Ca2+]i µM
Time (seconds)
K
0 mM Ca2+
2 mM Ca2+
Thapsigargin
[Ca2+]i µM
Time (seconds)
L
% SOCE
NS
shRNA: Scr
STX11: -
STX11 -
STX11 FHLH4
STX11 WT

Figure 2

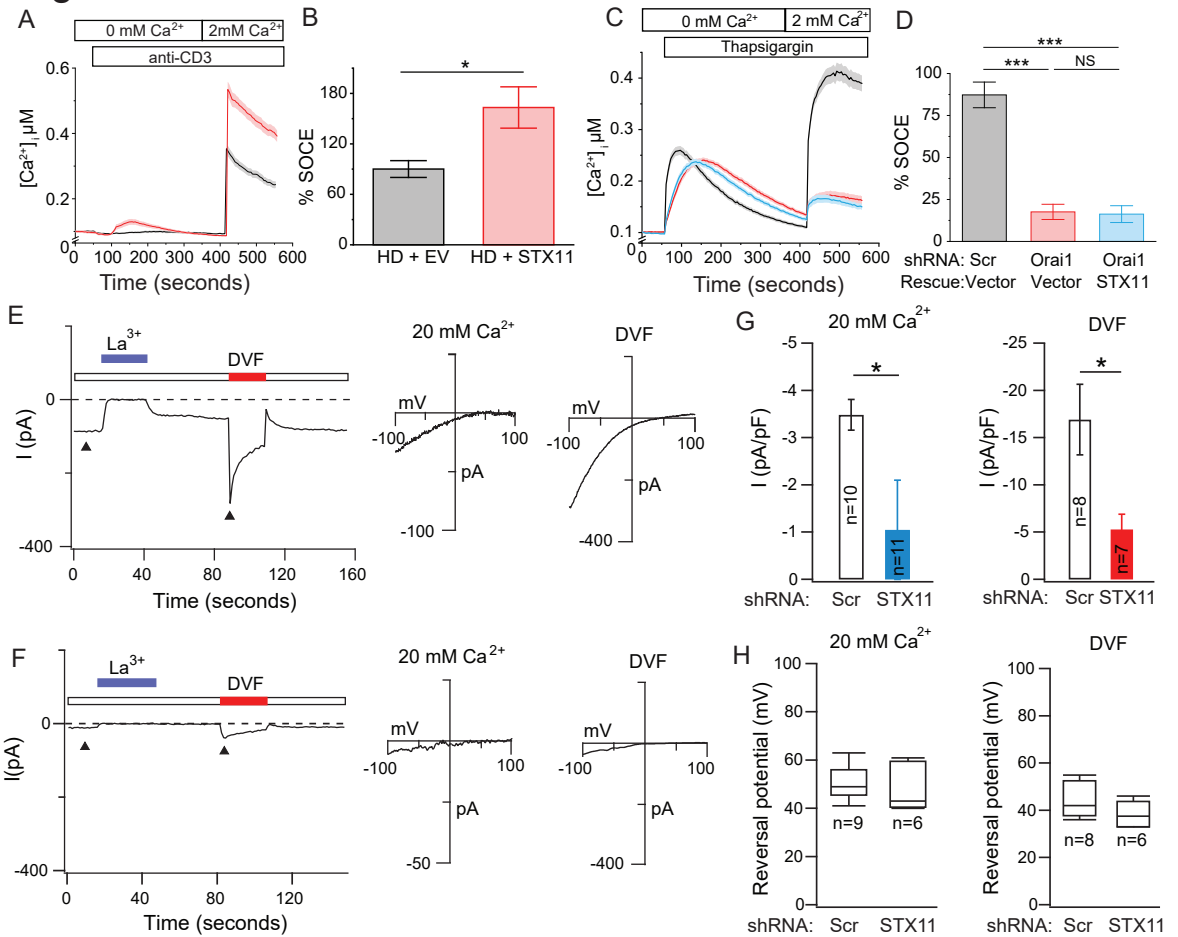
A
0 mM Ca2+
2mM Ca2+
anti-CD3
[Ca2+]i µM
Time (seconds)
B
% SOCE
HD + EV
HD + STX11
C
0 mM Ca2+
2 mM Ca2+
Thapsigargin
[Ca2+]i µM
Time (seconds)
D
% SOCE
shRNA: Scr
Rescue:Vector
Orai1
Vector
Orai1
STX11
NS
E
La3+
DVF
I (pA)
Time (seconds)
20 mM Ca2+
DVF
mV
pA
F
La3+
DVF
I(pA)
Time (seconds)
20 mM Ca2+
DVF
G
20 mM Ca2+
DVF
I (pA/pF)
n=10
n=11
n=8
n=7
shRNA: Scr STX11
H
20 mM Ca2+
DVF
Reversal potential (mV)
n=9
n=6
n=8
n=6
shRNA: Scr STX11

Figure 3

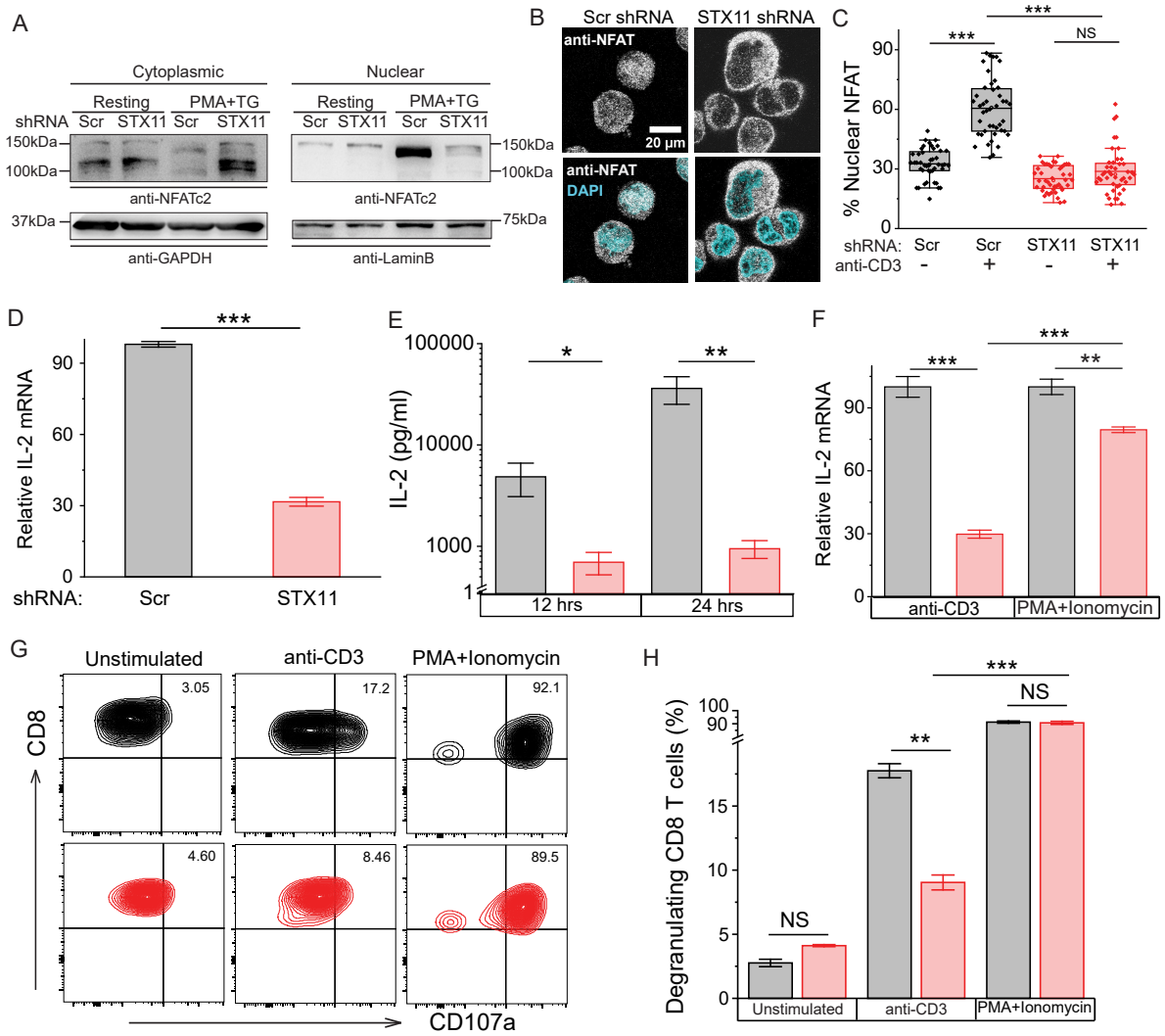
A
Cytoplasmic
Nuclear
Resting
PMA+TG
shRNA Scr STX11 Scr STX11
150kDa
100kDa
anti-NFATc2
37kDa
anti-GAPDH
75kDa
anti-LaminB
B
Scr shRNA
STX11 shRNA
anti-NFAT
20 µm
DAPI
C
% Nuclear NFAT
shRNA: Scr Scr STX11 STX11
anti-CD3 - + - +
NS
D
Relative IL-2 mRNA
shRNA: Scr STX11
E
IL-2 (pg/ml)
12 hrs
24 hrs
F
Relative IL-2 mRNA
anti-CD3
PMA+Ionomycin
G
Unstimulated
anti-CD3
PMA+Ionomycin
CD8
CD107a
3.05
17.2
92.1
4.60
8.46
89.5
H
Degranulating CD8 T cells (%)
Unstimulated
anti-CD3
PMA+Ionomycin
NS

Figure 4

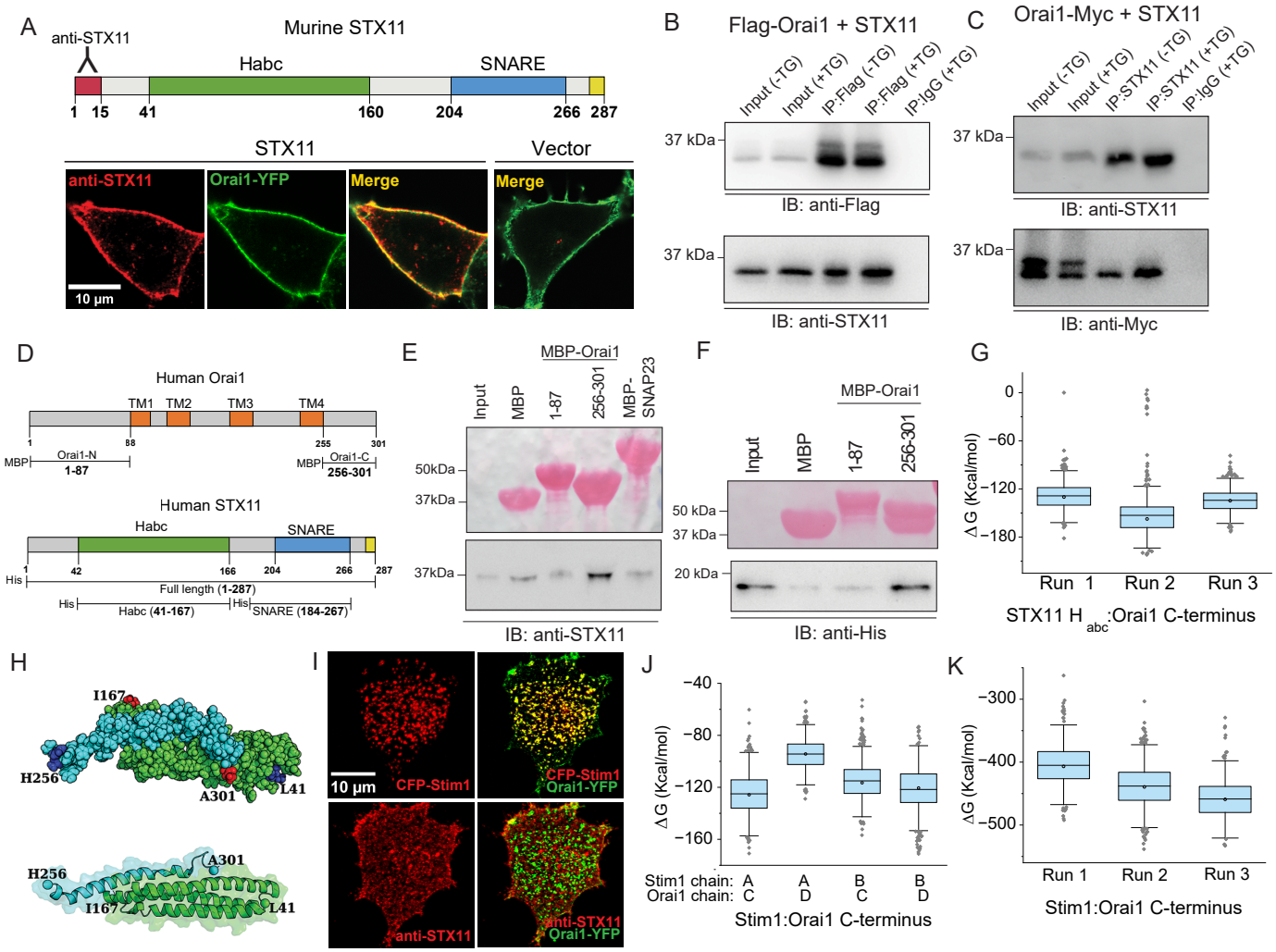
A
anti-STX11
Murine STX11
Habc
SNARE
1 15 41 160 204 266 287
STX11
Vector
anti-STX11
Orai1-YFP
Merge
Merge
10 µm
B
Flag-Orai1 + STX11
Input (-TG)
Input (+TG)
IP:Flag (-TG)
IP:Flag (+TG)
IP:IgG (+TG)
37 kDa
IB: anti-Flag
37 kDa
IB: anti-STX11
C
Orai1-Myc + STX11
Input (-TG)
Input (+TG)
IP:STX11 (-TG)
IP:STX11 (+TG)
IP:IgG (+TG)
37 kDa
IB: anti-STX11
37 kDa
IB: anti-Myc
D
Human Orai1
TM1 TM2 TM3 TM4
1 88 255 301
MBP Orai1-N 1-87
MBP Orai1-C 256-301
Human STX11
Habc
SNARE
1 42 166 204 266 287
His
Full length (1-287)
His
Habc (41-167)
His
SNARE (184-267)
E
MBP-Orai1
Input
MBP
1-87
256-301
MBP-SNAP23
50kDa
37kDa
37kDa
IB: anti-STX11
F
MBP-Orai1
Input
MBP
1-87
256-301
50 kDa
37 kDa
20 kDa
IB: anti-His
G
ΔG (Kcal/mol)
0
−60
−120
−180
Run 1
Run 2
Run 3
STX11 H abc:Orai1 C-terminus
H
I167
H256
A301
L41
H256
A301
I167
L41
I
10 µm
CFP-Stim1
CFP-Stim1
Orai1-YFP
anti-STX11
anti-STX11
Orai1-YFP
J
ΔG (Kcal/mol)
−40
−80
−120
−160
Stim1 chain: A A B B
Orai1 chain: C D C D
Stim1:Orai1 C-terminus
K
ΔG (Kcal/mol)
−300
−400
−500
Run 1
Run 2
Run 3
Stim1:Orai1 C-terminus

Figure 5

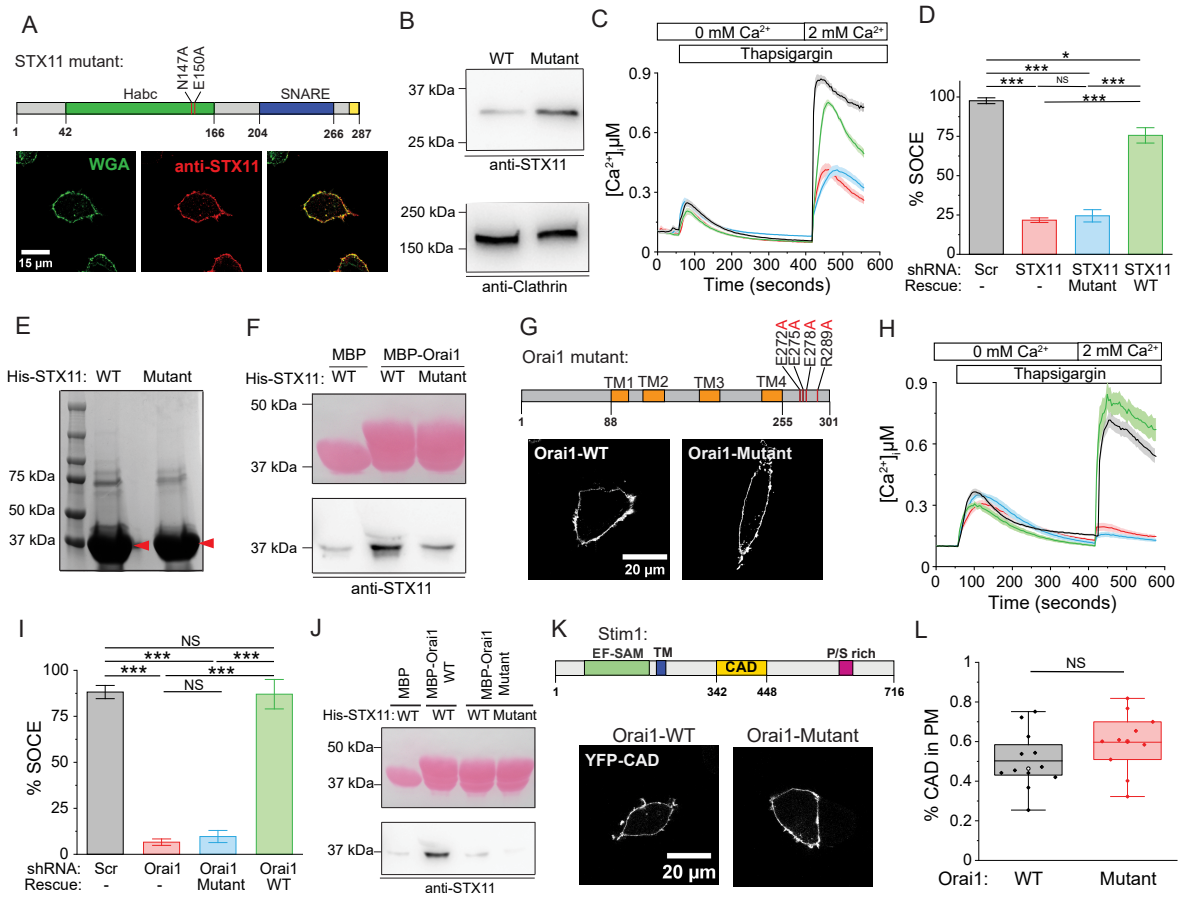
A
STX11 mutant:
N147A
E150A
Habc
SNARE
1
42
166
204
266
287
WGA
anti-STX11
15 µm
B
WT
Mutant
37 kDa
25 kDa
anti-STX11
250 kDa
150 kDa
anti-Clathrin
C
0 mM Ca2+
2 mM Ca2+
Thapsigargin
[Ca2+]µM
Time (seconds)
D
% SOCE
shRNA: Scr STX11 STX11 STX11
Rescue: - - Mutant WT
E
His-STX11: WT Mutant
75 kDa
50 kDa
37 kDa
F
MBP
MBP-Orai1
His-STX11: WT WT Mutant
50 kDa
37 kDa
anti-STX11
G
Orai1 mutant:
E272A
E275A
E278A
R289A
TM1 TM2 TM3 TM4
1
88
255
301
Orai1-WT
Orai1-Mutant
20 µm
H
0 mM Ca2+
2 mM Ca2+
Thapsigargin
[Ca2+]µM
Time (seconds)
I
% SOCE
shRNA: Scr Orai1 Orai1 Orai1
Rescue: - - Mutant WT
J
MBP
MBP-Orai1 WT
MBP-Orai1 Mutant
His-STX11: WT WT WT Mutant
50 kDa
37 kDa
anti-STX11
K
Stim1:
EF-SAM
TM
CAD
P/S rich
1
342
448
716
Orai1-WT
Orai1-Mutant
YFP-CAD
20 µm
L
% CAD in PM
Orai1: WT Mutant

Figure 6

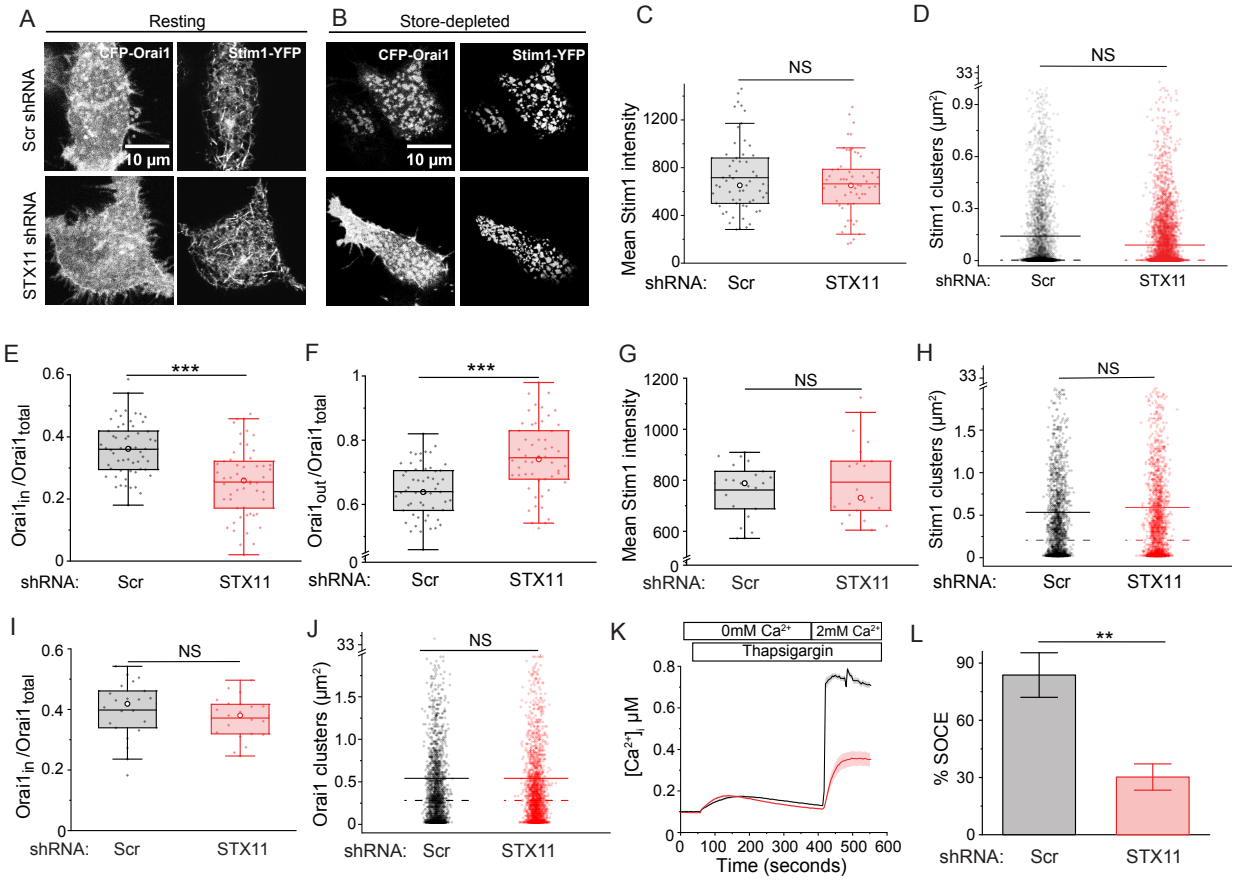
A
Resting
B
Store-depleted
CFP-Orai1
Stim1-YFP
Scr shRNA
STX11 shRNA
10 µm
C
D
NS
Mean Stim1 intensity
Stim1 clusters (µm²)
shRNA: Scr STX11
E
F
G
H
***
Orai1in /Orai1total
Orai1out /Orai1total
I
J
K
L
**
Orai1 clusters (µm²)
0mM Ca²⁺
2mM Ca²⁺
Thapsigargin
[Ca²⁺]i µM
Time (seconds)
% SOCE

Figure 7

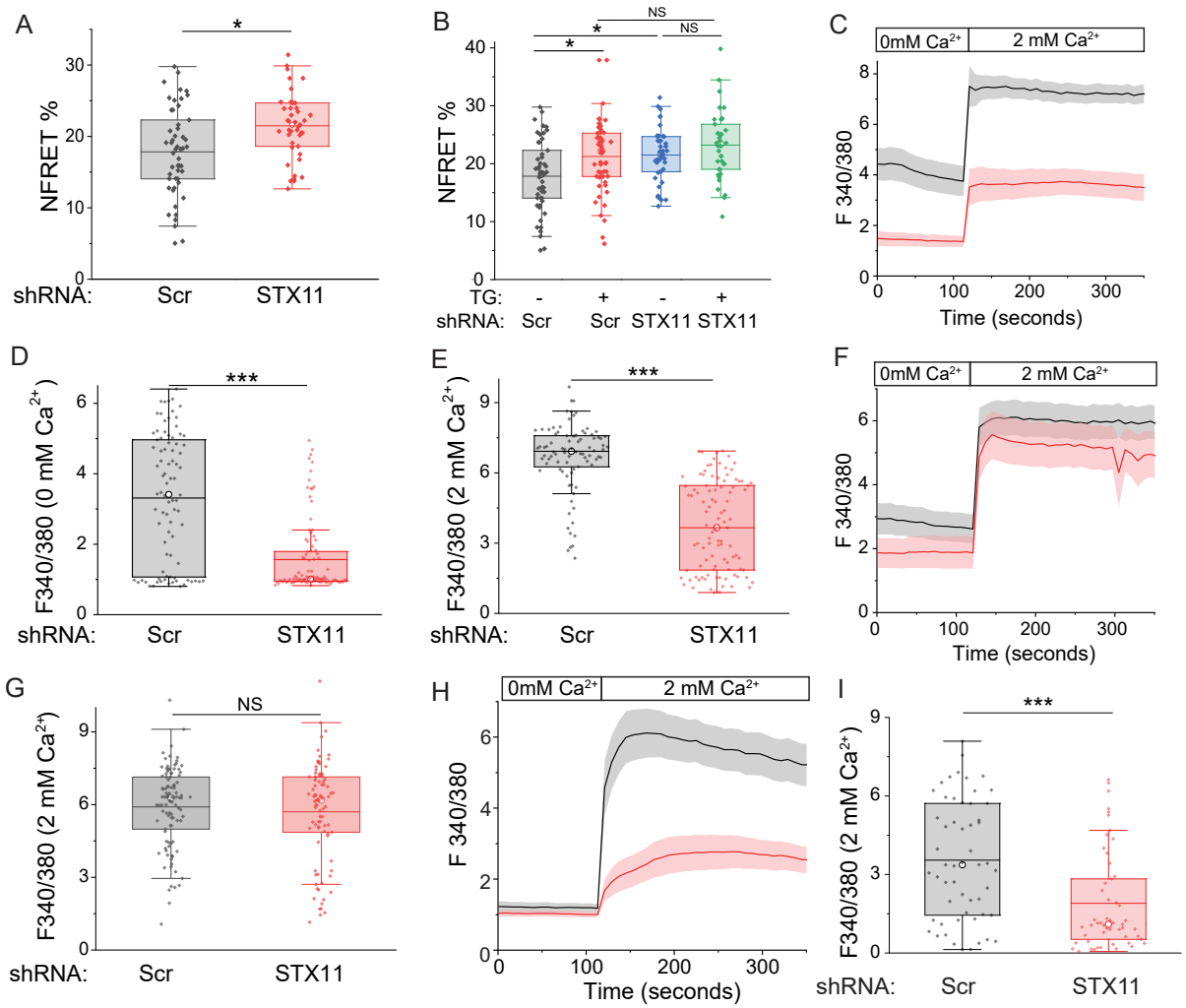
A
NFRET %
shRNA: Scr STX11
B
NFRET %
TG: - + - +
shRNA: Scr Scr STX11 STX11
NS
C
0mM Ca2+
2 mM Ca2+
F 340/380
Time (seconds)
D
F340/380 (0 mM Ca2+)
E
F340/380 (2 mM Ca2+)
F
G
H
I

J

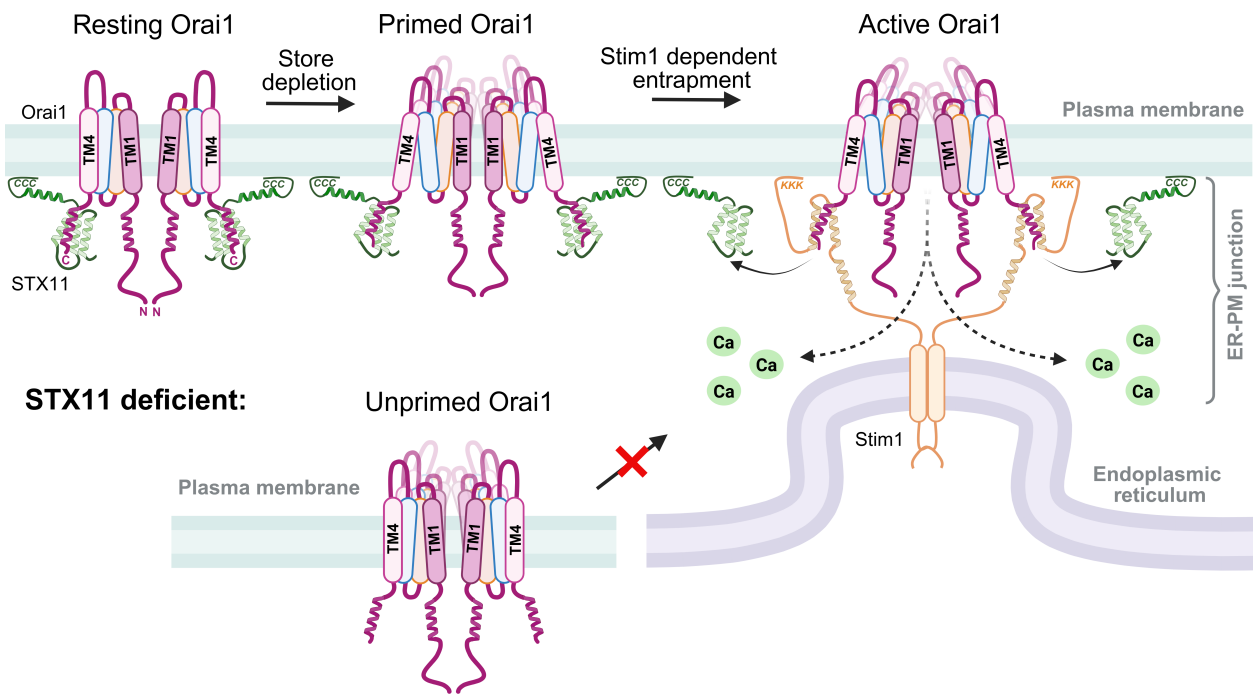
STX11 sufficient:
Resting Orai1
Store depletion
Primed Orai1
Stim1 dependent entrapment
Active Orai1
Orai1
TM4
TM1
STX11
Plasma membrane
KKK
Ca
ER-PM junction
Stim1
Endoplasmic reticulum
STX11 deficient:
Unprimed Orai1
Plasma membrane